



Scaled Spherical Simplex Filter and State-Space Damage-Plasticity Finite-Element Model for Computationally Efficient System Identification

M. Amir, S.M.ASCE¹; K. G. Papakonstantinou, M.ASCE²; and G. P. Warn, A.M.ASCE³

Abstract: This work presents an efficient online system identification approach by integrating a reduced sigma points—based filter with a high-fidelity mechanics-based state-space hysteretic finite-element modeling framework. The efficacy and computational efficiency of any sampling/sigma points—based nonlinear filtering process are conditional on the number of sigma/sample points required by the filter at each time step to quantify statistical properties of the involved quantities, as well as on the accuracy and computational cost of the underlying system model. A scaled spherical simplex filter (S3F) with a significantly decreased n + 2 sigma points set size is thus presented that is able to achieve similar robustness and accuracy as the state-of-the-art 2n + 1 sigma points unscented Kalman filter (UKF) for an n-dimensional state-space, yet with approximately 50% less computational requirements. The filtering framework is integrated with a recently developed fully parametrized damage plasticity—consistent hysteretic finite-element modeling approach that is able to account for distributed plasticity, axial-moment—shear interactions, and degradations in one unified formulation by employing the concepts of continuum damage mechanics and classical multiaxial plasticity. In the presented hysteretic model, the system matrices are constant and do not require updating throughout the analysis, whereas the degradations and inelasticity are updated through element-level hysteretic evolution equations in the form of resultant stress—strain laws. Overall, the system can be presented in a state-space form and can be solved with any first-order ordinary differential equation solver, without any linearization or gradient requirements, rendering the high-fidelity formulation robust and computationally efficient and enabling ideal compatibility in terms of computational implementation with the filtering methodology for online joint state-parameter identification. **DOI:** 10.1061/(ASCE)EM.1943-7889.0001945. © 2021 Ameri

Author keywords: Scaled spherical simplex filter; Online nonlinear filtering; Efficient uncertainty quantification and propagation; State-parameter identification; Hysteretic finite element; High-fidelity model; Damage-plasticity; State-space form; Bouc-Wen extension to FEM.

Introduction

This work focused on an online system identification framework, through the integration of a scaled spherical simplex filter (S3F), that is a sigma points—based nonlinear Kalman filtering approach, proposed by Papakonstantinou et al. (2022), with a fully parametrized damage plasticity—consistent hysteretic finite-element model presented in state-space form (Amir et al. 2020a, b, forthcoming).

Sigma points—based nonlinear Kalman filtering techniques require a predefined set of deterministic sigma points for uncertainty quantification and propagation, contrary to probabilistic sampling methods, e.g., particle filter (Gordon et al. 1993), or linearization approaches with gradient evaluation requirements, e.g., extended Kalman filter (Yun and Shinozuka 1980). The unscented Kalman filter (UKF), proposed by Julier et al. (1995) and Julier and Uhlmann

Note. This manuscript was submitted on October 5, 2020; approved on February 21, 2021; published online on November 17, 2021. Discussion period open until April 17, 2022; separate discussions must be submitted for individual papers. This paper is part of the *Journal of Engineering Mechanics*, © ASCE, ISSN 0733-9399.

(1996, 1997), and subsequently studied and analyzed by Wan and van der Merwe (2000) and van der Merwe (2004), among others, is a state-of-the-art and widely employed sigma points-based Kalman filtering technique for identification of nonlinear structural systems, as shown by Chatzi et al. (2010), Song and Dyke (2014), Astroza et al. (2015), Erazo and Hernandez (2016), Chatzis and Chatzi (2017), Astroza et al. (2017), and Song et al. (2020), among many other works, owing its widespread use to its ease of implementation, accuracy, computational stability, and efficiency (van der Merwe 2004).

The UKF requires 2n + 1 sigma points for uncertainty quantification and propagation for a *n*-dimensional state space, and offers second-moment accuracy for any input distribution. Higher-order accuracy can be achieved by increasing the number of sigma points, but with an increased computational demand of the filtering process, e.g., skewed/third-moment approaches, conjugate unscented transform, or higher order filters (Julier 1998; Adurthi et al. 2018; Tenne and Singh 2003), because the computational cost of the filtering process is directly proportional to the number of sigma points. Recognizing this, Julier and Uhlmann (2002) and Julier (2003) suggested reduced asymmetric n + 2 sigma point sets to quantify statistical properties of *n*-dimensional random variables. These methods could significantly reduce the computational burden, particularly for large-dimensional systems; however, the spread of the points and the skewness effects pose instability issues, particularly with increasing dimensions (Julier 2002; Julier and Uhlmann 2004).

Based on our recently proposed S3F approach (Papakonstantinou et al. 2022), the identification framework in the present work

¹Graduate Student Researcher, Dept. of Civil and Environmental Engineering, Pennsylvania State Univ., University Park, PA 16802. Email: mza40@psu.edu

²Associate Professor, Dept. of Civil and Environmental Engineering, Pennsylvania State Univ., University Park, PA 16802 (corresponding author). Email: kpapakon@psu.edu

³Associate Professor, Dept. of Civil and Environmental Engineering, Pennsylvania State Univ., University Park, PA 16802. Email: gpw1@psu.edu

overcomes the aforementioned limitations by appropriately allocating n+2 sigma points and determining suitable scaling and weight parameters, and therefore achieves similar accuracy and robustness as the UKF while reducing the computational requirement by nearly 50%. The S3F was introduced by Papakonstantinou et al. (2022), and combines all the best attributes of the previous approaches, i.e., the computational efficiency of the n+2 sigma points, along with the accuracy and robustness of the UKF.

Computational efficiency of the identification scheme was further improved in this work by integrating the filtering framework with our recently developed fully parametrized damage plasticityconsistent hysteretic finite-element model (Amir et al. 2020a, b, forthcoming). The suggested finite-element framework was derived based on the generalized multiaxial hysteretic stress-strain laws by following the fundamentals of the uniaxial Bouc-Wen type smooth hysteretic models, but with multiaxial interactions and consistent degradations, while satisfying all the classical plasticity postulates (as shown in the Appendix). Smooth hysteretic uniaxial Bouc-Wen models, proposed by Bouc (1967) and Wen (1976), and later employed and modified by many researchers (e.g., Baber and Wen 1981; Baber and Noori 1985; Foliente 1995; Sivaselvan and Reinhorn 2000; Wang et al. 2001; Papakonstantinou et al. 2008) to expand their features, including degrading/nondegrading and asymmetric properties, have been employed extensively in a range of applications for simulating nonlinear structural components, devices, and materials response, as summarized by Ismail et al. (2009). Due to the important property of these models in expressing the nonlinearity/hysteresis through a single parametrized first-order nonlinear ordinary differential equation (ODE), they have been aptly and commonly adopted in nonlinear filtering applications (e.g., Wu and Smyth 2008; Chatzi et al. 2010; Xie and Feng 2012; Song and Dyke 2014; Chatzis et al. 2015; Kontoroupi and Smyth 2016; Erazo and Hernandez 2016; Chatzis and Chatzi 2017; Olivier and Smyth 2017; Song 2018; Calabrese et al. 2018; Lei et al. 2019). All the aforementioned works employed simplified mass springtype single or multiple degrees-of-freedom (DOF) structural system models, in which the nonlinearity is governed by Bouc-Wen models due to their implementational compatibility in state-space form. However, such simplified models are not able to reflect or simulate detailed local response of the structure that needs to be obtained through higher-fidelity nonlinear modeling techniques, such as solid finite-elements and fiber-based approaches, among others (Spacone et al. 1996; Filippou and Fenves 2004; Scott et al. 2008; Deierlein et al. 2010; Lignos and Krawinkler 2011), thereby limiting their application for structural identification. Recent contributions for finite-element model updating using Bayesian techniques, including UKF, were provided by Al-Hussein and Haldar (2015), Astroza et al. (2015, 2017), and Song et al. (2020), in which mechanics-based high-fidelity finite-element models were employed for frame-type nonlinear structures, to simulate detailed global and local structural responses. However, these finite-element identification methods did not incorporate complex structural component-level degradation phenomena in the identification process, and often were based on system parameter estimation in an offline manner.

This work combined the accuracy of high-fidelity mechanics-based finite-element models, incorporating multiaxial degradation-plasticity phenomena, with the computational advantages and nonlinear filtering capabilities offered by Bouc-Wen approaches, to achieve efficient joint state-parameter identification in an online framework. Amir et al. (2020a) developed a consistent and efficient hysteretic finite-element model in which new displacement/rotation/hysteretic interpolation fields are derived to satisfy the exact equilibrium and kinematic conditions of a nonlinear Timoshenko beam element. Degradation effects were introduced in

Amir et al. (2020b) by treating strength degradation as a scalar damage function and employing continuum damage theory principles (Kachanov 1958, 1980; Lemaitre 1996) to satisfy the plasticity postulates for a degrading system. Amir et al. (forthcoming) presented a computationally efficient solution scheme in state-space form for dynamic analysis, inspired by the formulations of Triantafyllou and Koumousis (2011, 2012), in which the system matrices are not required to be updated and the entire framework is presented elegantly by a system of ODEs that can be solved without the need for linearizations or gradient requirements. In addition to the accuracy and efficiency of this high-fidelity finite-element framework, the state-space formulation, similar to any Bouc—Wen type nonlinear system, is directly compatible with the filtering process for online state-parameter identification.

Overall, the presented system identification approach achieves computational efficiency (1) through the filtering process, by reducing the number of model calls from 2n + 1 per step as with the traditional UKF to n + 2 with the S3F, and (2) by integrating the filter with an efficient and accurate high-fidelity degrading hysteretic finite-element model enabling online identification, which offers computational benefits due to the direct use of stress resultants at the section level, constant matrices avoiding system-level matrix update and inversion, and the use of first-order ODE solvers without gradient evaluation requirements during the solution process. This paper presents a detailed description of the S3F and the finite-element model, and illustrates through numerical examples the capabilities of the identification approach, related to complex nonlinear degrading systems, time-variant parameters, dual state estimation and parameter identification, online estimations, and sparse measurement data.

Scaled Spherical Simplex Filter

In the context of the presented formulation, the problem of estimating the hidden states of a nonlinear dynamic system, given noisy observation data, can be expressed in the following state-space form:

$$\mathbf{x}_{k} = \mathbf{f}(\mathbf{x}_{k-1}, \mathbf{q}_{k}, \mathbf{v}_{k}, \mathbf{\theta})$$

$$\mathbf{u}_{k} = \mathbf{h}(\mathbf{x}_{k}, \mathbf{r}_{k}, \mathbf{v}_{k}, \mathbf{\theta})$$
(1)

where Eq. (1) presents a first-order hidden Markov model with \mathbf{f} and $\mathbf{h} =$ deterministic state update and measurement equations; $\mathbf{u} =$ observed state; $\mathbf{x} =$ hidden state vector; $\mathbf{v} =$ exogenous input; $\mathbf{\theta} =$ parameter vector that parametrizes functions \mathbf{f} and \mathbf{h} ; \mathbf{q} and $\mathbf{r} =$ process and observation noises, respectively; and subscript k = discrete time step. In a probabilistic framework, the objective is to recursively update the posterior density $p(\mathbf{x}_k | \underline{\mathbf{u}}_{1:k})$ of the system state, given the observation set, $\underline{\mathbf{u}}_{1:k} = \{\underline{\mathbf{u}}_1, \underline{\mathbf{u}}_2, \dots, \underline{\mathbf{u}}_k\}$, through the following classical Bayes' rule and Chapman–Kolmogorov equation, respectively:

$$p(\mathbf{x}_{k}|\underline{\mathbf{u}}_{1:k}) = \frac{p(\underline{\mathbf{u}}_{k}|\mathbf{x}_{k})p(\mathbf{x}_{k}|\underline{\mathbf{u}}_{1:k-1})}{\int p(\underline{\mathbf{u}}_{k}|\mathbf{x}_{k})p(\mathbf{x}_{k}|\underline{\mathbf{u}}_{1:k-1})d\mathbf{x}_{k}}$$
$$p(\mathbf{x}_{k}|\underline{\mathbf{u}}_{1:k-1}) = \int p(\mathbf{x}_{k}|\mathbf{x}_{k-1})p(\mathbf{x}_{k-1}|\underline{\mathbf{u}}_{1:k-1})d\mathbf{x}_{k-1}$$
(2)

where $p(\mathbf{x}_{k-1}|\underline{\mathbf{u}}_{1:k-1}) = \text{known posterior density at time index } (k-1);$ and $p(\mathbf{x}_k|\mathbf{x}_{k-1})$ and $p(\underline{\mathbf{u}}_k|\mathbf{x}_k) = \text{state transition probability density and measurement likelihood functions, respectively, that can be determined through the state update and measurement equations in Eq. (1). For a general nonlinear system, the multidimensional integrals in Eq. (2) do not have closed forms, and approximate methods are required for uncertainty propagation and recursive posterior updates, e.g., linearization, Monte Carlo$

sampling, or unscented transformations, among other approaches (Wan and van der Merwe 2000). The unscented transformation, which is the primary focus of the present work, tracks only the posterior mean $\hat{\mathbf{x}}_k = E[\mathbf{x}_k | \underline{\mathbf{u}}_{1:k}]$ and covariance \mathbf{P}_k at each time step k, by capturing $p(\mathbf{x}_k | \mathbf{x}_{k-1})$ and $p(\underline{\mathbf{u}}_k | \mathbf{x}_k)$ in the form of the first two statistical moments, through a predefined set of sigma points, and is a core component of the overall filter implementation.

Selection of Sigma Points and Scaling Effects

The unscented transformation for the UKF requires 2n+1 symmetrically placed sigma points, for an n-dimensional state space, such that the 2n points are placed on a hypersphere of radius $\alpha\sqrt{n}$ and the remaining sigma point is located at the origin/center, in a standard normal space (c-space), with zero mean and identity covariance matrix. The sigma points then can be obtained in the original space through an affine transformation, $\mathbf{x} = \bar{\mathbf{x}} + \sqrt{\mathbf{P_{xx}}}\mathbf{c}$, to capture the first two statistical moments, i.e., mean and covariance ($\bar{\mathbf{x}}$, $\mathbf{P_{xx}}$), of a multivariate random variable \mathbf{x} , where \mathbf{c} represents a sigma point in standard normal space. The resulting set of the sigma points propagates through the nonlinear function, $\mathbf{y} = \mathbf{f}(\mathbf{x})$, to evaluate the updated mean and covariance ($\bar{\mathbf{y}}$, $\mathbf{P_{yy}}$) of the transformed random variable \mathbf{y} . Overall, the unscented transformation for the UKF can be expressed as (Wan and van der Merwe 2000)

$$\begin{split} W_{0}^{(m)} &= 1 - \frac{1}{\alpha^{2}}; \quad W_{0}^{(c)} = 1 - \frac{1}{\alpha^{2}} + (1 - \alpha^{2} + \beta); \\ W_{i}^{(m)} &= W_{i}^{(c)} = \frac{1}{2\alpha^{2}n} \quad i = 1, \dots, 2n; \\ \mathbf{X}_{0} &= \bar{\mathbf{x}}; \quad \mathbf{X}_{i} = \bar{\mathbf{x}} \pm (\alpha\sqrt{n})(\sqrt{\mathbf{P}_{\mathbf{x}\mathbf{x}}})_{i} \quad i = 1, \dots, 2n; \\ \mathbf{Y}_{i} &= \mathbf{f}(\mathbf{X}_{i}); \quad \bar{\mathbf{y}} = \sum_{i=0}^{2n} W_{i}^{(m)} \mathbf{Y}_{i}; \quad \mathbf{P}_{\mathbf{y}\mathbf{y}} = \sum_{i=0}^{2n} W_{i}^{(c)} [\mathbf{Y}_{i} - \bar{\mathbf{y}}] [\mathbf{Y}_{i} - \bar{\mathbf{y}}]^{T} \end{split}$$

$$(3)$$

where (m) = mean; (c) = covariance; \mathbf{X}_i and $\mathbf{Y}_i = \text{sigma points corresponding to random variables } \mathbf{x}$ and \mathbf{y} , respectively; $W_i = \text{associated weights}$; and α and $\beta = \text{scaling factors}$. A sought objective, as previously mentioned, was to reduce the computational effort of the filtering process through the reduction in the number of sigma points while achieving similar accuracy as the UKF.

Papakonstantinou et al. (2022) proposed a scaled spherical simplex filter (S3F) that requires only n + 2 sigma points for

the unscented transformation and achieves similar accuracy and robustness as the UKF. The minimum set of sigma points that can be used to provide a nonsingular covariance is n + 1 (Julier and Uhlmann 2002). However, the n + 1 sigma points cannot achieve the same order of accuracy and robustness as the UKF. To take advantage of the scaling parameter α , and to preserve important features of the classical UKF, one more sigma point can be added to this minimum set at the origin/center, just as in the case of the scaled UKF, and the remaining n + 1 points then can be placed on a hypersphere of radius $\alpha \sqrt{n}$ in the standard normal space. The scaling factor α determines the spread of the sigma points and can suppress the errors associated with third and higher moments. The sigma points in the standard normal space are shown in Fig. 1 for both the UKF and S3F. Based on Fig. 1, the resulting sigma points matrix for a *n*-dimensional system in the *c*-space is formulated as (Papakonstantinou et al. 2022)

$$\mathbf{C} = [\mathbf{C}_{0} \dots \mathbf{C}_{n+1}] = \begin{bmatrix} 0 & -\frac{q_{1}}{1} & q_{1} & 0 & \cdots & 0 & 0 \\ 0 & -\frac{q_{2}}{2} & -\frac{q_{2}}{2} & q_{2} & \cdots & 0 & 0 \\ \vdots & \vdots & \vdots & \vdots & \ddots & \vdots & \vdots \\ 0 & -\frac{q_{n}}{n} & -\frac{q_{n}}{n} & -\frac{q_{n}}{n} & \cdots & -\frac{q_{n}}{n} & q_{n} \end{bmatrix}$$
where $q_{t} = \alpha \sqrt{\frac{t(n+1)}{t+1}}$ for $t \in [1, 2, \dots, n]$ (4)

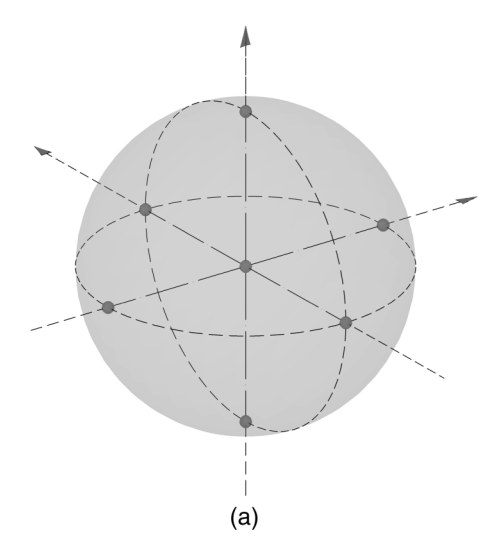
where C = matrix of size (n, n + 2), consisting of n + 2 sigma point vectors, C_i , each of size n, with $i \in [0, 1, ..., n + 1]$. The unscented transformation, using the n + 2 sigma points matrix C, for the S3F is summarized as (Papakonstantinou et al. 2022)

$$W_{0}^{(m)} = 1 - \frac{1}{\alpha^{2}}; \quad W_{0}^{(c)} = 1 - \frac{1}{\alpha^{2}} + (1 - \alpha^{2} + \beta);$$

$$W_{i}^{(m)} = W_{i}^{(c)} = \frac{1}{\alpha^{2}(n+1)} \quad i = 1, ..., n+1;$$

$$\mathbf{X}_{i} = \bar{\mathbf{x}} + (\sqrt{\mathbf{P}_{xx}}\mathbf{C})_{i} \quad i = 0, ..., n+1;$$

$$\mathbf{Y}_{i} = \mathbf{f}(\mathbf{X}_{i}); \quad \bar{\mathbf{y}} = \sum_{i=0}^{n+1} W_{i}^{(m)}\mathbf{Y}_{i}; \quad \mathbf{P}_{yy} = \sum_{i=0}^{n+1} W_{i}^{(c)}[\mathbf{Y}_{i} - \bar{\mathbf{y}}][\mathbf{Y}_{i} - \bar{\mathbf{y}}]^{T}$$
(5)



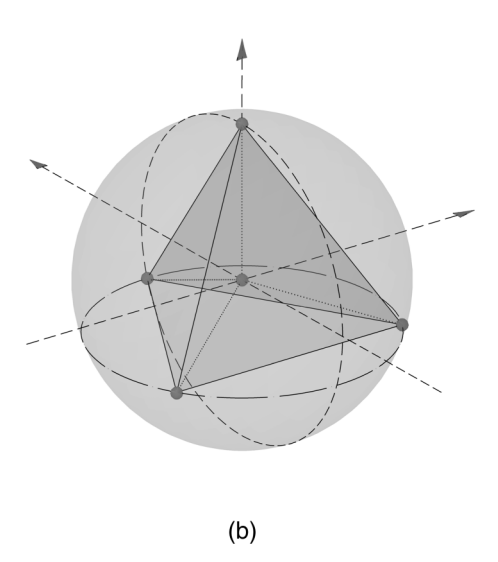


Fig. 1. Sigma points locations on a sphere of radius $\alpha \sqrt{n}$ (n=3), in three-dimensional c-space, for (a) UKF; and (b) S3F.

where scaling parameter β incorporates potential output distribution information relating to its fourth moments, similar to the UKF. The equivalent accuracy between the UKF and the S3F is attributed mainly to the scaling factor α . For the UKF, a small value of the parameter suppresses the errors associated with fourth and higher moments, with odd moments being inherently zero due to symmetric sigma points distribution. Therefore, the UKF provides secondmoment accuracy for any prior distribution and third-moment accuracy for symmetric priors. Due to the asymmetric distribution of sigma points in the S3F, not all odd moments are zero in this case, however, a small value of α , in the range 0.01–0.0001, can result in negligible contributions of third and higher moments, thereby nearly achieving second-moment accuracy for any distribution and thirdmoment accuracy for symmetric priors, exactly similar to the UKF, even with this reduced asymmetric sigma points selection. Moreover, the role of parameter β is also equivalent in the two approaches, that is, to incorporate partial fourth moments, and therefore a typical value of 2 is selected without any prior information about the distribution (Wan and van der Merwe 2000; Papakonstantinou et al. 2022).

Filter Implementation

Based on the posterior mean and covariance $(\hat{\mathbf{x}}_{k-1}, \mathbf{P}_{k-1})$ estimates at the (k-1)th time step, n+2 sigma points \mathbf{X}_{k-1} are selected, as shown previously, and are transformed through the state update equation in Eq. (1), resulting in a new set of sigma points $\mathbf{X}_{k|k-1}$, which then are employed to obtain the prior mean and covariance $(\hat{\mathbf{x}}_k^-, \mathbf{P}_k^-)$ at the kth time step as follows:

$$\mathbf{X}_{k|k-1} = \mathbf{f}[\mathbf{X}_{k-1}, \mathbf{v}_{k}, \mathbf{\theta}] \qquad \hat{\mathbf{x}}_{k}^{-} = \sum_{i=0}^{n+1} W_{i}^{(m)} \mathbf{X}_{i,k|k-1}$$

$$\mathbf{P}_{k}^{-} = \sum_{i=0}^{n+1} W_{i}^{(c)} [\mathbf{X}_{i,k|k-1} - \hat{\mathbf{x}}_{k}^{-}] [\mathbf{X}_{i,k|k-1} - \hat{\mathbf{x}}_{k}^{-}]^{T} + \mathbf{Q}_{k}$$
(6)

where \mathbf{Q}_k is the process noise covariance matrix. From the apriori estimates $(\hat{\mathbf{x}}_k^-, \mathbf{P}_k^-)$, the $\mathbf{X}_{k|k-1}$ sigma points are redrawn and transformed through the measurement equation in Eq. (1), again resulting in another new set of sigma points $\mathbf{U}_{k|k-1}$, which then are used to estimate the measurement mean and covariance $(\hat{\mathbf{u}}_k^-, \mathbf{P}_{u_k u_k})$ and the state-measurement cross-covariance matrix $\mathbf{P}_{x_k u_k}$. Finally, with the available observation set, $\underline{\mathbf{u}}_k$, at the kth time step, the posterior mean and covariance $(\hat{\mathbf{x}}_k, \mathbf{P}_k)$ are updated through the Kalman gain, $\mathbf{K}_k = \mathbf{P}_{x_k u_k} \mathbf{P}_{u_k^- u_k}^{-1}$. The overall process is expressed as

$$\mathbf{U}_{k|k-1} = \mathbf{h}(\mathbf{X}_{k|k-1}, \mathbf{v}_{k}, \mathbf{\theta})
\mathbf{\hat{u}}_{k}^{-} = \sum_{i=0}^{n+1} W_{i}^{(m)} \mathbf{U}_{i,k|k-1}
\mathbf{P}_{u_{k}u_{k}} = \sum_{i=0}^{n+1} W_{i}^{(c)} [\mathbf{U}_{i,k|k-1} - \hat{\mathbf{u}}_{k}^{-}] [\mathbf{U}_{i,k|k-1} - \hat{\mathbf{u}}_{k}^{-}]^{T} + \mathbf{R}_{k}
\mathbf{P}_{x_{k}u_{k}} = \sum_{i=0}^{n+1} W_{i}^{(c)} [\mathbf{X}_{i,k|k-1} - \hat{\mathbf{x}}_{k}^{-}] [\mathbf{U}_{i,k|k-1} - \hat{\mathbf{u}}_{k}^{-}]^{T}
\mathbf{\hat{x}}_{k} = \hat{\mathbf{x}}_{k}^{-} + \mathbf{K}_{k} (\underline{\mathbf{u}}_{k} - \hat{\mathbf{u}}_{k}^{-}); \quad \mathbf{P}_{k} = \mathbf{P}_{k}^{-} - \mathbf{K}_{k} \mathbf{P}_{u_{k}u_{k}} \mathbf{K}_{k}^{T}$$
(7)

where \mathbf{R}_k = observation noise covariance matrix.

Damage-Plasticity State-Space Finite-Element Model

Amir et al. (2020b) developed a fully parametrized damage-plasticity finite-element model that is able to simulate highly nonlinear structural behavior. Although the presented hysteretic finite-element was derived based on the concepts of damage mechanics and can incorporate degradations and interactions while satisfying all the multiaxial classical plasticity postulates, as shown in the Appendix, the model's implementation is straightforward and analogous to a typical Bouc–Wen model (Table 1). In Table 1, the second column lists the uniaxial hysteretic Bouc–Wen equations with scalar variables, and the third column lists the corresponding multiaxial finite-element expressions for the Timoshenko beam element with coupled degradation-plasticity, where the vectors and matrices are indicated with bold characters for the multiaxial representation.

In the force-displacement expression of the uniaxial case (Table 1, second column), F is the force, $\bar{\alpha}$ is the kinematic hardening, d is the displacement, and z is the hysteretic deformation. Similarly, in the equilibrium expression of the finite-element model (Table 1, third column), F represents the element nodal forces in the local coordinate system, consisting of axial force, shear force, and moment at the start and end nodes of the beam element; K and H are the constant element stiffness and hysteretic matrices, respectively (defined in the Appendix), analogous to $\bar{\alpha}k$ and $(1-\bar{\alpha})k$ of the uniaxial case; and d and z correspond to displacement and hysteretic DOF vectors respectively, where $\mathbf{d} = \{u_1 \ w_1 \ \theta_1 \ u_2 \ w_2 \ \theta_2\}^T$ consists of axial deformation u, transverse deformation w, and rotation θ , at the start and end nodes of the element, indicated by subscripts 1 and 2, respectively, and $\mathbf{z} = \{\mathbf{z}_{(x=0)}^T \mathbf{z}_{(x=L)}^T\}^T$ consists of hysteretic deformations, at the start and end nodes, obtained by substituting x = 0 and x = L respectively in the subscript (x) of the

Table 1. Bouc-Wen to hysteretic beam finite-element model

Equation categories	Uniaxial Bouc-Wen	Hysteretic beam finite-element
Force-displacement and evolution equations	$F = \bar{\alpha}kd + (1 - \bar{\alpha})kz$	$\mathbf{F} = \mathbf{K}\mathbf{d} + \mathbf{H}\mathbf{z}$
	$\dot{z} = \frac{1}{\eta} (1 - \nu H_1 H_2) \dot{d}$	$\dot{\mathbf{z}}_{(x)} = \mathbf{\eta}^{-1}[(\mathbf{I} - \bar{H}_1 \bar{H}_2 \bar{\mathbf{R}}) \dot{\boldsymbol{\epsilon}} - \dot{\boldsymbol{\nu}} \mathbf{z}]_{(x)}$
Components of evolution equations	$H_1 = z ^m$ $H_2 = a + b \operatorname{sgn}(z\dot{d})$	$egin{aligned} ar{H}_1 &= \Phi(ar{\mathbf{P}}^h) + 1 ^m \ ar{H}_2 &= a + b \mathrm{sgn}[(ar{\mathbf{P}}^h)^T \dot{oldsymbol{arepsilon}}] \end{aligned}$
		$\bar{\mathbf{R}} = \left[\left(\frac{\partial \Phi}{\partial \bar{\mathbf{P}}^h} \right)^T \mathbf{D} \left(\frac{\partial \Phi}{\partial \bar{\mathbf{P}}^h} \right) \right]^{-1} \left[\left(\frac{\partial \Phi}{\partial \bar{\mathbf{P}}^h} \right) \left(\frac{\partial \Phi}{\partial \bar{\mathbf{P}}^h} \right)^T \mathbf{D} \right]$
		$\Rightarrow \bar{H}_1, \bar{H}_2, \bar{\mathbf{R}} = \mathbf{g}(\mathbf{d}, \mathbf{z})$
Strength and stiffness degradations	$\nu = 1 + \delta_{\nu}[\exp(\delta_{\nu n}e) - 1]$ $\eta = 1 + \delta_{\eta}e$	$oldsymbol{ u} = \mathbf{I} + \delta_{ u} [\exp(\delta_{ u n} \mathbf{e}) - \mathbf{I}] onumber \ \mathbf{\eta} = \mathbf{I} + \delta_{\eta} \mathbf{e}$

hysteretic evolution equation, for an element of length L. Furthermore, the evolution equations for the hysteretic deformations in both uniaxial and multiaxial cases are presented in the form of first-order ODEs, where in the finite-element framework, $\boldsymbol{\varepsilon}_{(x)} = \{\varepsilon_u \, \varepsilon_\gamma \, \varepsilon_\phi\}_{(x)}^T$ and $\mathbf{z}_{(x)} = \{z_u \, z_\gamma \, z_\phi\}_{(x)}^T$ are the section-level strain and hysteretic deformation vectors at a distance (x) from the start node of the beam element. In the uniaxial evolution equations, ν and η are the strength and stiffness degradation functions respectively, whereas for the multiaxial case, $\mathbf{v} = \mathrm{diag}(\nu_u, \nu_\gamma, \nu_\phi)$ and $\mathbf{\eta} = \mathrm{diag}(\eta_u, \eta_\gamma, \eta_\phi)$ are the diagonal matrices consisting of strength and stiffness degradation functions for axial, shear, and bending components.

In the second row of Table 1, describing the components of the evolution equations, the functions H_1 and H_2 of the uniaxial Bouc– Wen model are smooth in the range [0,1] and Heaviside functions, respectively, similar to the functions \bar{H}_1 and \bar{H}_2 . However, these latter are defined differently because the finite-element model expressions were derived to incorporate consistent degradations and interactions, as shown in the Appendix. Related to this, interaction matrix, $\bar{\mathbf{R}}$, is also included in the finite-element framework, contrary to the uniaxial case. Overall, \bar{H}_1 , \bar{H}_2 , and $\bar{\mathbf{R}}$ are functions of the effective hysteretic force, $\bar{\mathbf{P}}^h = \mathbf{v}_{(x)} \mathbf{P}^h_{(x)} = (\mathbf{I} - \bar{\boldsymbol{\alpha}}) \mathbf{D} \mathbf{v}_{(x)} \mathbf{z}_{(x)}$, and the yield/interaction surface, $\Phi = \Phi(\bar{\mathbf{P}}^h)$. In the aforementioned effective force expression, $\bar{\mathbf{\alpha}} = \operatorname{diag}(\alpha_u, \alpha_\gamma, \alpha_\phi)$ and $\mathbf{D} =$ $diag(EA, GA_s, EI)$ are the strain hardening and rigidity matrices, respectively; E and G are the elastic and shear modulus; A and A_s are the total area and effective shear area, respectively; and Iis the section moment of inertia. Based on the expressions of the yield criterion, effective hysteretic force, and the strain vector, the functions \bar{H}_1 and \bar{H}_2 and matrix $\bar{\mathbf{R}}$ eventually can be expressed in terms of displacement and hysteretic deformation vectors, similar to the uniaxial case. This is also indicated in the third column of Table 1, in which $\mathbf{g}(\cdot)$ represents the resulting function after applying necessary transformations. For both formulations, a, b, and m are the hysteretic model parameters, and $sgn(\cdot)$ is a signum function. Parameter m controls the smoothness of the transition from the elastic to the inelastic regime, whereas a and b control the shape of the hysteretic loops.

The last row of Table 1 lists degradation functions for both cases, in which e is the hysteretic energy dissipation, given as $\dot{e}=(1-\bar{\alpha})kz\dot{d}$, and $\mathbf{e}=\mathrm{diag}(e_u,e_\gamma,e_\phi)$ is a diagonal matrix consisting of hysteretic energy components corresponding of axial, shear, and flexural deformations, respectively; δ_ν and δ_η are accordingly the constant strength and stiffness degradation parameters; and the parameter $\delta_{\nu n}$ is used to normalize the energy dissipation, and controls the nonlinear evolution of the strength degradation. The presented formulation uses the nonlinear strength degradation function derived by Amir et al. (2020b) to simulate the structural behavior; however, a linear function or other variants can be also used as needed. In addition, softening behavior, degradation asymmetry, and pinching phenomena can be included straightforwardly for both uniaxial and finite-element cases, as shown by Amir et al. (2020b), depending on the model requirements.

Overall, based on Table 1, it is evident that the hysteretic finite-element can be presented concisely in the form of first-order ODE evolution equations, similar to typical Bouc-Wen type systems, and thus is well suited for filtering applications and online dual state-parameter identification. Therefore, unlike the traditional nonlinear finite-element formulation, in this case any ODE solver scheme can be used straightforwardly, e.g., the family of Runge-Kutta methods, without the requirement of gradient evaluation or linearization for the system level matrix updates, as presented

by Amir et al. (2020b, forthcoming). In addition, due to the parametrized behavior of the finite-element, the same model can be applied for different element types, ranging from flexure dominant to shear dominant to bracing members, and can simulate diverse phenomena, including linear, nonlinear, degradation, softening, and pinching, through a single unified formulation, thereby representing a general framework.

For the finite-element model in Table 1, global element matrices are obtained as $\mathbf{K}_g = \mathbf{\Lambda}^T \mathbf{K} \mathbf{\Lambda}$, and $\mathbf{H}_g = \mathbf{\Lambda}^T \mathbf{H}$, based on the typical coordinate transformation (Bathe 2014), where $\mathbf{\Lambda}$ is the standard coordinate transformation matrix. The overall system force-displacement expression, after global matrix assembly and applying appropriate boundary conditions, is obtained as

$$\mathbf{F}_S = \mathbf{K}_S \mathbf{d}_S + \mathbf{H}_S \mathbf{z}_S \tag{8}$$

where \mathbf{K}_S and \mathbf{H}_S = constant system level matrices, which do not require updating throughout the analysis; \mathbf{F}_S = system nodal force; and \mathbf{d}_S and \mathbf{z}_S = system-level displacement and hysteretic DOF vectors, respectively, such that \mathbf{z}_S is obtained by appending all the element-level hysteretic DOFs.

Numerical Examples

Two numerical example cases are presented based on the expressions in Table 1 for online state-parameter identification of nonlinear degrading systems. The first example case is a mass–spring–dashpot system which treats nonlinearity and degradations through the uniaxial hysteretic model expressions in the second column of Table 1, whereas the second example case is a hysteretic finite-element model identification following the element-level formulation presented in the third column of Table 1 and the resulting system-level framework in Eq. (8). Detailed derivation of the hysteretic finite-element model development and system-level formulation can be seen in Amir et al. (2020a, b, forthcoming). For both example cases, the equation of motion of the system subjected to dynamic excitation is expressed as

$$\mathbf{M}_{S}\ddot{\mathbf{d}}_{S} + \mathbf{C}_{S}\dot{\mathbf{d}}_{S} + \underbrace{\mathbf{K}_{S}\mathbf{d}_{S} + \mathbf{H}_{S}\mathbf{z}_{S}}_{\mathbf{F}_{S}} = \mathbf{F}(t)$$
(9)

where \mathbf{M}_S , \mathbf{C}_S , \mathbf{K}_S , and \mathbf{H}_S = system mass, damping, stiffness, and hysteretic matrices, respectively; and $\mathbf{F}(t)$ = excitation vector related to the input ground acceleration in these examples. To be consistent with the filtering framework, and for the purpose of dual state-parameter estimations, the overall system in Eq. (9) can be presented in the following state-space form, in which all the unknown parameters are augmented in the state vector, in order to be identified by the filtering process:

$$\begin{cases}
\dot{\mathbf{d}}_{S} \\
\dot{\mathbf{d}}_{S}
\end{cases} = \begin{bmatrix}
\mathbf{0} & \mathbf{I} & \mathbf{0} \\
-\mathbf{M}_{S}^{-1}\mathbf{K}_{S} & -\mathbf{M}_{S}^{-1}\mathbf{C}_{S} & -\mathbf{M}_{S}^{-1}\mathbf{H}_{S}
\end{bmatrix} \begin{pmatrix}
\dot{\mathbf{d}}_{S} \\
\dot{\mathbf{d}}_{S} \\
\mathbf{z}_{S}
\end{pmatrix} + \begin{pmatrix}
\mathbf{0} \\
\mathbf{M}_{S}^{-1}\mathbf{F}(t)
\end{pmatrix}; \dot{\mathbf{z}}_{S} = \mathbf{f}(\mathbf{d}_{S}, \mathbf{z}_{S}, \mathbf{\theta}); \dot{\mathbf{\theta}} = \mathbf{0} \quad (10)$$

where function \mathbf{f} is obtained based on the evolution equation in Table 1 for either the mass–spring–dashpot model or the finite-element system; and $\mathbf{\theta} =$ unknown parameter vector to be identified. The overall state-parameter vector for the online dual identification scheme can thus be expressed as $\mathbf{x} = \{\mathbf{d}_{S}^T \ \dot{\mathbf{d}}_{S}^T \ \mathbf{z}_{S}^T \ \mathbf{\theta}^T\}^T$.

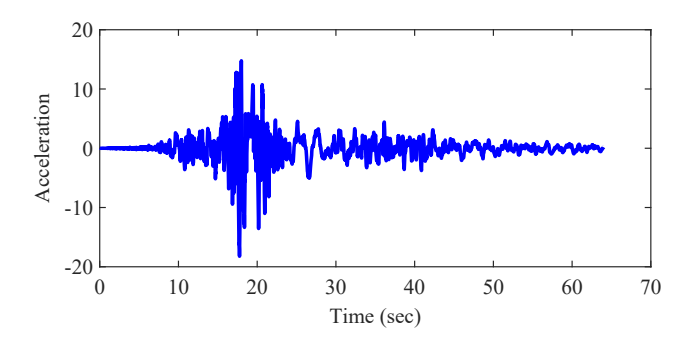


Fig. 2. Seismic excitation without added noise for the mass–spring–dashpot system.

Online Identification of Hysteretic Degrading Mass-Spring-Dashpot System

The efficacy of the S3F was examined by comparing its response with that of the UKF for the identification of a 20-DOF nonlinear and degrading mass–spring–dashpot system, subjected to the scaled Chi-Chi seismic excitation in Fig. 2. The system matrices and DOF vectors in the state-space expressions of Eq. (10) are given as

$$\mathbf{M}_{S} = \begin{bmatrix} \bar{m}_{1} & 0 & \cdots & 0 \\ 0 & \bar{m}_{2} & \cdots & 0 \\ \vdots & \vdots & \ddots & 0 \\ 0 & 0 & 0 & \bar{m}_{20} \end{bmatrix}$$

$$\mathbf{C}_{S} = \begin{bmatrix} \bar{c}_{1} + \bar{c}_{2} & -\bar{c}_{2} & \cdots & 0 \\ -\bar{c}_{2} & \bar{c}_{2} + \bar{c}_{3} & \cdots & 0 \\ \vdots & \vdots & \ddots & -\bar{c}_{20} \\ 0 & 0 & -\bar{c}_{20} & \bar{c}_{20} \end{bmatrix}$$
(11)

$$\mathbf{K}_{S} = \begin{bmatrix} k_{1}^{e} + k_{2}^{e} & -k_{2}^{e} & \cdots & 0 \\ -k_{2}^{e} & k_{2}^{e} + k_{3}^{e} & \cdots & 0 \\ \vdots & \vdots & \ddots & -k_{20}^{e} \\ 0 & 0 & -k_{20}^{e} & k_{20}^{e} \end{bmatrix}$$

$$\mathbf{H}_{S} = \begin{bmatrix} k_{1}^{h} - k_{2}^{h} & 0 & \cdots & 0 & 0 \\ 0 & k_{2}^{h} & -k_{3}^{h} & \cdots & 0 & 0 \\ \vdots & \vdots & \vdots & \ddots & 0 & 0 \\ 0 & 0 & 0 & 0 & k_{19}^{h} & -k_{20}^{h} \\ 0 & 0 & 0 & 0 & 0 & k_{20}^{h} \end{bmatrix}$$

$$k_{i}^{e} = \bar{\alpha}_{i}\bar{k}_{i}, \quad k_{i}^{h} = (1 - \bar{\alpha}_{i})\bar{k}_{i} \quad \text{for } i = [1, 2, \dots, 20];$$

$$\mathbf{d}_{S} = \{d_{1}d_{2} \dots d_{20}\}^{T}; \; \mathbf{z}_{S} = \{z_{1}z_{2} \dots z_{20}\}^{T}$$

$$(12)$$

where \bar{m}_i , \bar{k}_i , \bar{c}_i , and $\bar{\alpha}_i$ = mass, stiffness, damping, and kinematic hardening coefficients, respectively; and d_i and z_i = displacement and hysteretic deformations corresponding to the *i*th DOF. In this example, all the coefficients, parameters, and associated input/output responses, including mass, damping, hardening, hysteretic/degradation parameters, seismic excitation, and displacements, are unitless to represent any general framework, and the mass is an identity matrix. Nonlinearity is considered in the first two DOFs of the

system by specifying $\bar{\alpha}_i=0$ for $i\in[1,2]$ and $\bar{\alpha}_i=1$ otherwise, and is associated with the uniaxial hysteretic model in Table 1. The parameters to be identified are the stiffness ($\bar{\mathbf{k}}=\{\bar{k}_1\bar{k}_2\dots\bar{k}_{20}\}$) and damping coefficients ($\bar{\mathbf{c}}=\{\bar{c}_1\bar{c}_2\dots\bar{c}_{20}\}$) for all DOFs, and hysteretic (a,b,m) and degradation parameters $(\delta_{\eta},\delta_{\nu})$ corresponding to the nonlinear DOFs, assuming $\delta_{\nu n}=0.01$. The true values of the damping parameters are $\bar{c}_1=\dots=\bar{c}_5=0.3$, $\bar{c}_6=\dots=\bar{c}_{10}=0.4$, $\bar{c}_{11}=\dots=\bar{c}_{15}=0.5$, and $\bar{c}_{16}=\dots=\bar{c}_{20}=0.6$; the stiffness parameters are $\bar{k}_1=\dots=\bar{k}_5=18$, $\bar{k}_6=\dots=\bar{k}_{10}=16$, $\bar{k}_{11}=\dots=\bar{k}_{15}=15$, $\bar{k}_{16}=\dots=\bar{k}_{18}=14$, and $\bar{k}_{19}=\bar{k}_{20}=13$; the hysteretic Bouc–Wen parameters are a=1, b=2, and m=2 for both nonlinear DOFs; and the degradation parameters are $\delta_{\eta}=1$ and $\delta_{\nu}=2$.

The unknown parameter vector to be identified in Eq. (10) is thus expressed as $\mathbf{\theta} = \{ \, \mathbf{\bar{c}} \quad \mathbf{\bar{k}} \quad a \quad b \quad m \quad \delta_{\eta} \quad \delta_{\nu} \, \}^T ,$ resulting in the augmented state vector, $\mathbf{x} = \{ \mathbf{d}_S^T \ \dot{\mathbf{d}}_S^T \ \mathbf{z}_S^T \ \boldsymbol{\theta}^T \}^T$ with n = 105. Therefore, based on the number of sigma points, the UKF evaluates the underlying model [Eq. (10)] 211 times/step, whereas the S3F requires only 107 model evaluations at each time step. For the identification process, the values of the filter scaling parameters α and β are equal to 0.001 and 2, respectively, for both the S3F and the UKF. Arbitrary values are assigned for the process noise and observation noise matrices and are given as $\mathbf{Q}_k = diag(0.0001\mathbf{v}_k^2)$, with nonzero diagonal elements only corresponding to the $\dot{\mathbf{d}}_S$ state, and \mathbf{R}_k $0.003\,\mathbf{I}$, where \mathbf{v}_k is the acceleration input and \mathbf{I} is the identity matrix, whereas the initial covariance, which is dependent on the uncertainty of the initial states/parameters, is assigned as P_0 = $diag((0.2\hat{\mathbf{x}}_0)^2 + 0.001)$, where $\hat{\mathbf{x}}_0$ is the initial state vector. For the observation data, acceleration measurements are considered for all DOFs, and the input and observation data are all contaminated with zero-mean white Gaussian noise with a 3% signal-to-noise ratio (SNR) to simulate highly noisy but realistic scenarios.

The estimation results for both filters are given in Figs. 3–6. Fig. 3 shows the dynamic states of the system corresponding to nonlinear DOFs; Fig. 4 shows the stiffness and damping coefficients for all DOFs; Fig. 5 corresponds to the smooth Bouc–Wen parameters a, b, and m; and Fig. 6 shows the identified degradation parameters. In Figs. 3(c and d), the effect of nonlinearity, strength and stiffness degradations are evident, particularly in the first DOF. Figs. 4(c and d) include error plots to show clearly that all the story stiffness and damping parameters are converging to their respective true values. Both filters performed notably well and largely converged to the true values within the first 30 s of the input excitation. Importantly, the S3F exhibited the same performance as the UKF for both state and parameter identification, but with a reduced computational cost of nearly 50%.

To further test the robustness of the filters, the complexity of the identification scheme was increased for the same mass-springdashpot system by also considering time-variant parameters, assuming a limited number of available measurements, and identifying all the hysteretic and degradation parameters for both nonlinear DOFs distinctly, indicated now by subscripts 1 and 2, such that the total hysteretic/degradation parameters to be identified become 10. The stiffness parameters for the third and fourth DOFs were abruptly reduced at the 20th second of the seismic excitation during the data generation process, something which was not modeled during identification. The practical concept is based on the assumption that the system might undergo damage and stiffness loss in DOFs where it is not expected and modeled a priori with appropriate nonlinear formulations, for example, as used for DOFs 1 and 2. Measurement sparsity is accordingly considered by assuming acceleration data to be available now at alternating DOFs, from 1 to 19, resulting in 10 measurements. Some of the hysteretic/degradation parameters for the second DOF were varied now, compared with the previous example,

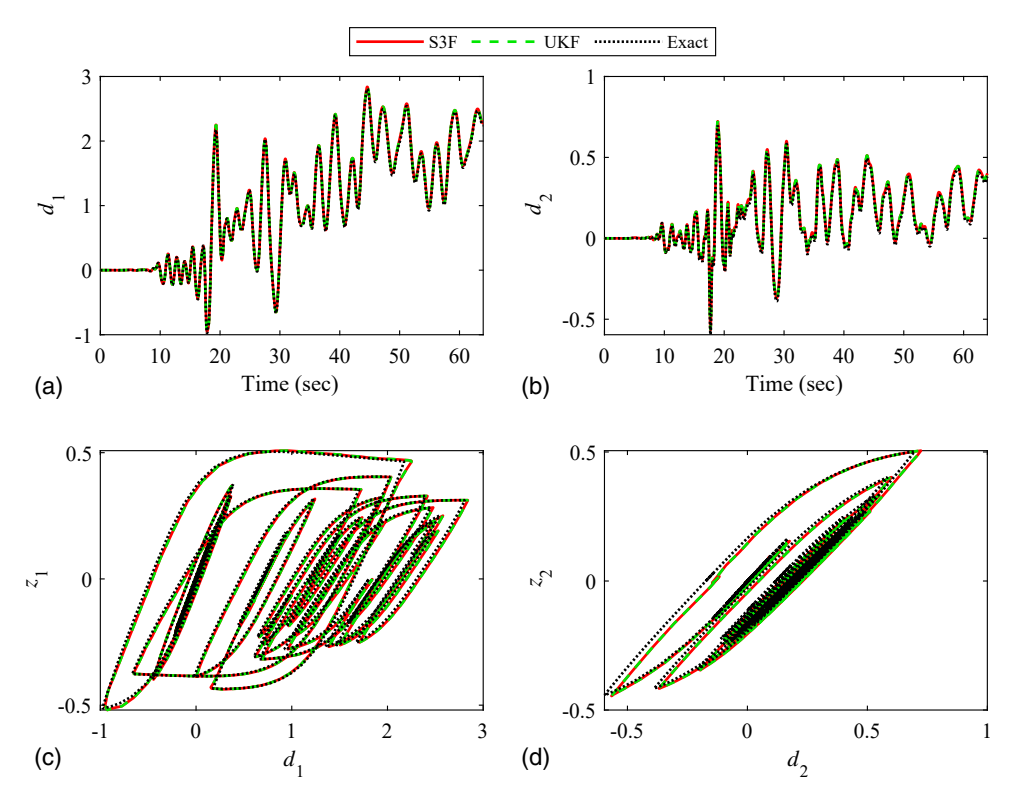


Fig. 3. Dynamic state estimation using S3F and UKF for a 20-DOF degrading nonlinear system with 3% SNR and acceleration measurements.

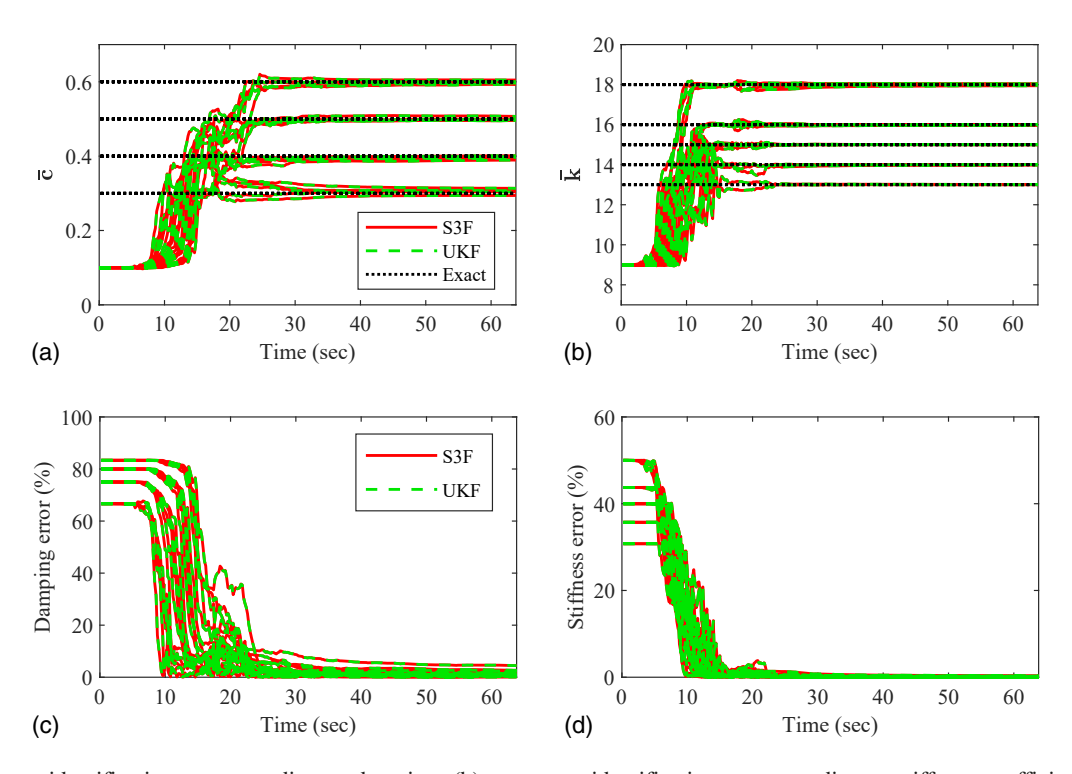


Fig. 4. (a) Parameter identification corresponding to damping; (b) parameter identification corresponding to stiffness coefficients; and (c and d) corresponding error plots.

for illustration purposes and to enhance nonlinearity and degradations in this DOF (Figs. 7–10), whereas all other relevant parameters remain the same. Results again showed that both filters performed well and in the same manner, particularly with respect

to the dynamic states (Fig. 7), noting also that the second DOF was completely unobserved. The filtering performance with respect to parameter identification slightly deteriorated compared with the previous case, due to the significant complexity increase of the

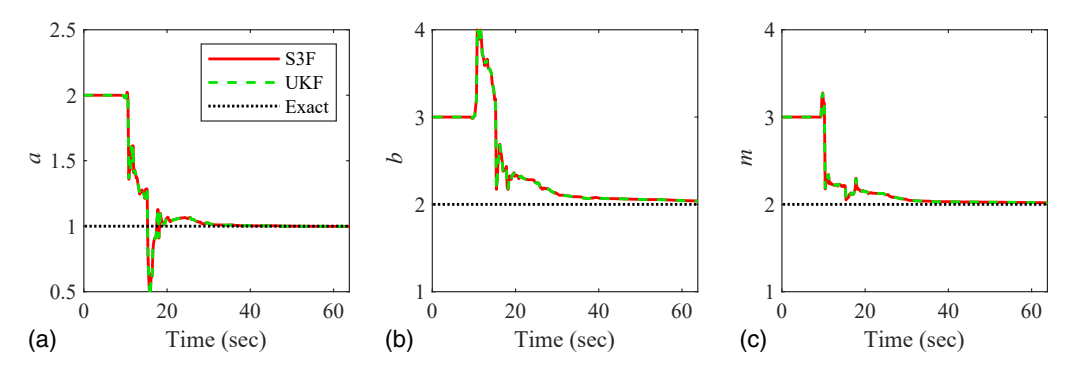


Fig. 5. Hysteretic parameters identification.

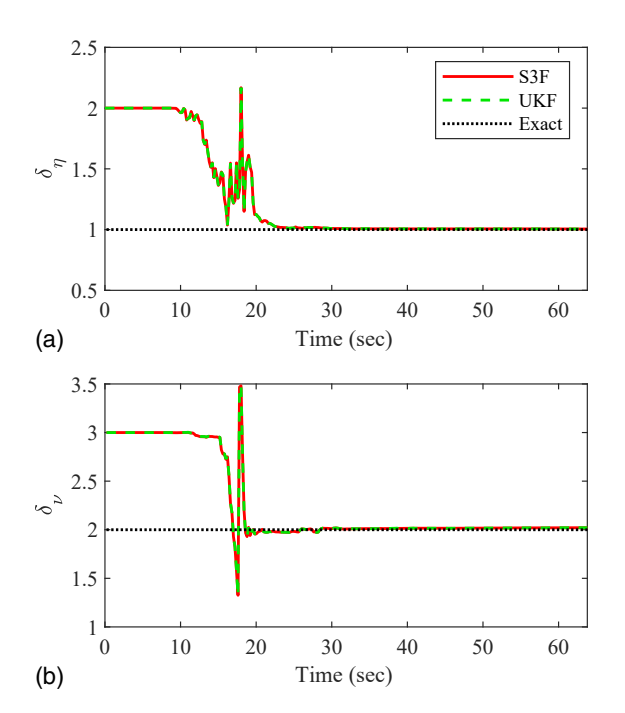


Fig. 6. Stiffness and strength degradation parameters identification.

problem (Figs. 8–10). Furthermore, the stiffness coefficients for all DOFs [Fig. 8(b)], both before and after the decrease, were correctly identified by the filters, as also indicated in Figs. 8(c and d) for the first four DOFs exhibiting nonlinearity and stiffness drop.

Online Identification of Degrading Hysteretic Finite-Element Frame System

This indicative example case of a three-story four-bay steel braced frame structure (Fig. 11), comprising different element types, e.g., shear-dominant, flexure-dominant, and brace elements, demonstrated a range of complex nonlinear and degrading phenomena with interaction and distributed plasticity, and illustrated the efficacy of the S3F for online joint state-parameter identification of a high-fidelity finite-element model with sparse and noisy acceleration measurement data. The structure was subjected to the seismic base excitation obtained using the stochastic ground motion simulation approach of Vlachos et al. (2018) (Fig. 12). All the beam elements were W24×76, brace elements were HSS4X4X1/4, whereas the interior and exterior column elements were W30 × 173 and W14 × 190, respectively. All elements had a yield strength of 290 MPa, elastic modulus of 210 GPa, and shear modulus of

77 GPa. To obtain the nodal mass matrix, the floor mass was assumed to be 30 t/unit length. Axial moment–shear interaction was considered using the Gendy and Saleeb criterion (Gendy and Saleeb 1993). A considerable 3% zero-mean white Gaussian noise level was added in this example for both the input excitation in Fig. 12 and all utilized acceleration measurement responses, with the assumption that horizontal accelerations were available only at the locations indicated in Fig. 11.

Based on the mechanical and geometrical properties of the elements, the system matrices and most of the hysteretic parameters can be obtained, including the elastic modulus, shear modulus, cross-section area, shear area, moment of inertia, and plastic section capacities. In addition, the postelastic to elastic stiffness ratio or else the kinematic hardening component was assumed to be $\alpha_u =$ $\alpha_{\gamma} = \alpha_{\phi} = 0.002$. To ensure that the elastic unloading and loading branches had the same slope, a and b were both assigned equal to 0.5, whereas the $\delta_{\nu n}$ parameter was assumed to be 5×10^{-6} for beams and columns, and 5×10^{-5} for the brace elements. Consequently, the unknown parameters in this example were the strength degradation, stiffness degradation, and inelastic transition for each structural member, and can describe the entire hysteresis of the element, with the strength degradation controlling the plastic region and/or the yield capacity, the stiffness degradation controlling the elastic loading-reloading-unloading slope, and the inelastic transition controlling the transition smoothness from elastic to inelastic regime for both loading and unloading branches. These parameters are to be identified for all elements of the system, resulting in $3N_{el}$ total unknown parameters for the identification process, with $\mathbf{\theta} = \{m, \delta_{\nu}, \delta_{\eta}\}_{i \in [1, 2, \dots, N_e]}$, such that $\{m, \delta_{\nu}, \delta_{\eta}\}_i$ are the parameters corresponding to the ith element, and N_{el} is the number of elements in the system. In this example, three parameters corresponding to each element were identified, to illustrate the identification potential of the combined modeling-filtering approach. However, in real applications, assumptions can be made to group these parameters for multiple elements to further simplify the problem and reduce the number of identified parameters. The parameters and the hysteretic states in this example had consistent scales for dual state-parameter identification. For the present example, the dimension of the resulting augmented state vector \mathbf{x} was n = 351, where DOFs corresponding to $(\mathbf{d}_S, \dot{\mathbf{d}}_S)$ and \mathbf{z}_S were 90 and 174 $(=6N_{el})$, respectively, and the parameters to be identified were 87 (= $3N_{el}$). Therefore, the UKF required 703 (= 2n + 1) sigma points/step, whereas the S3F required only 353 (= n + 2) points, thereby again improving the computational efficiency by nearly 50%. The scaling factors values of $\alpha = 0.01$ and $\beta = 2$ were used herein for both the UKF and S3F, and the relevant matrices used were $\mathbf{P_0} = \operatorname{diag}((0.1\hat{\mathbf{x}}_0)^2 + 0.00001)$, where $\hat{\mathbf{x}}_0$ is the initial state

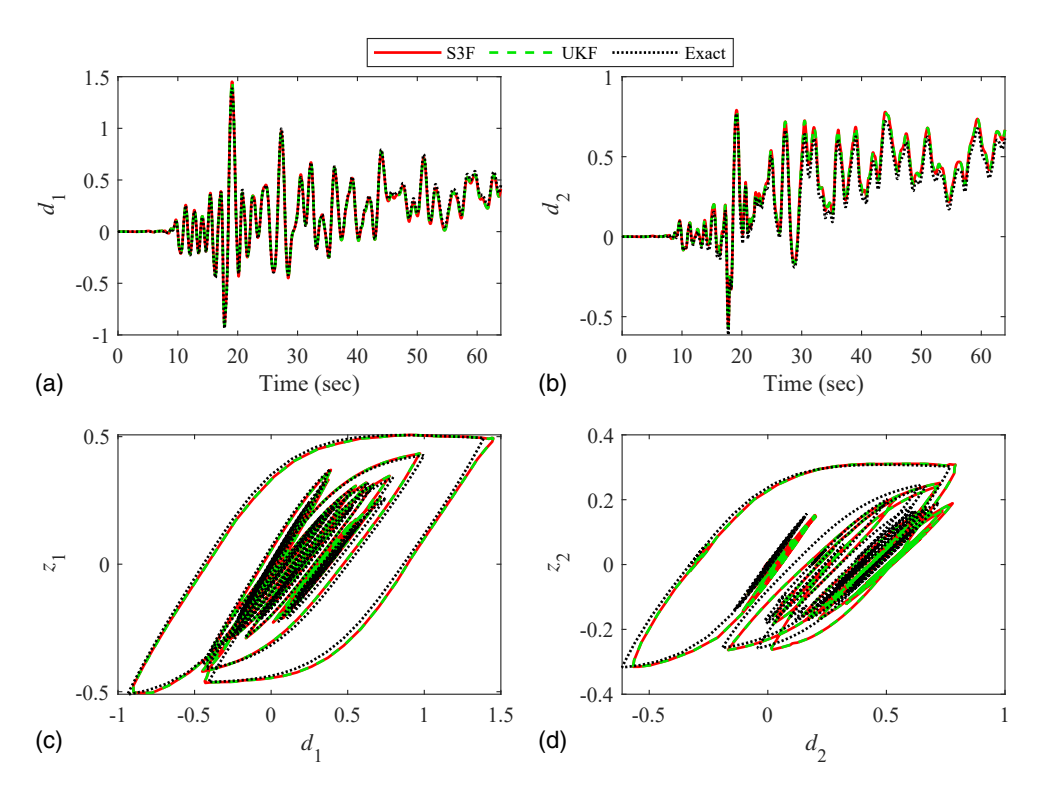


Fig. 7. Dynamic state estimation using S3F and UKF for a 20-DOF degrading nonlinear system with 3% SNR, time-variant parameters, and sparse acceleration measurements.

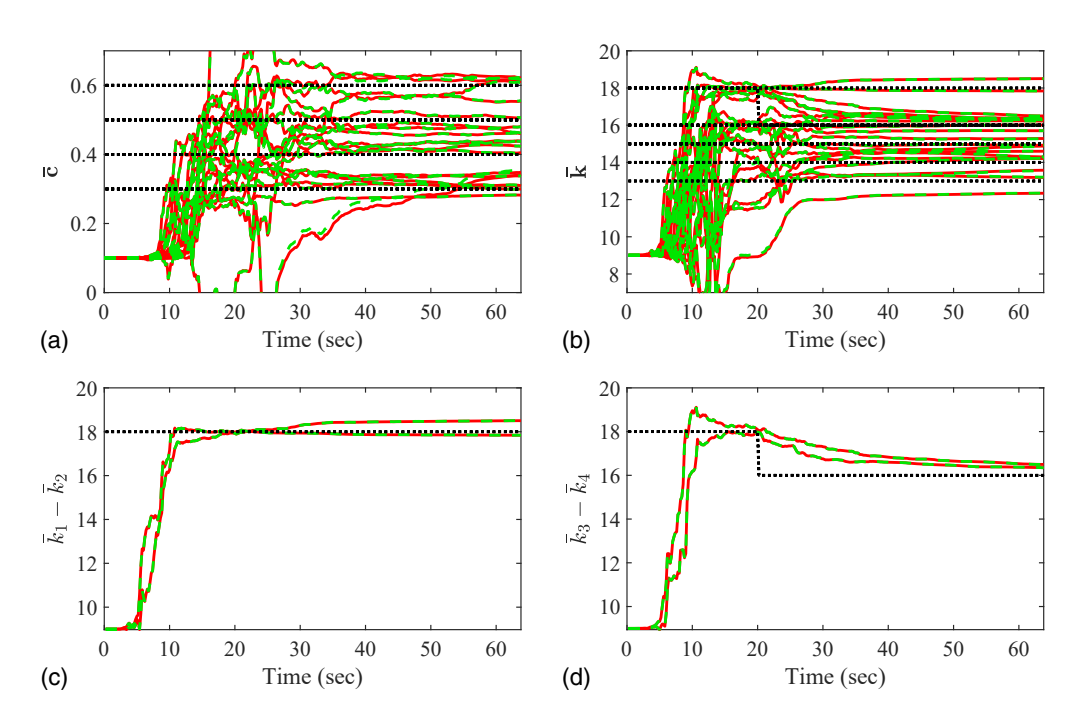


Fig. 8. (a) Damping coefficients for all DOFs; (b) stiffness coefficients for all DOFs; (c) stiffness coefficients for DOFs 1 and 2; and (d) stiffness coefficients for DOFs 3 and 4.

vector; $\mathbf{Q}_k = \text{diag}(0.00001\mathbf{v}_k^2)$, with nonzero diagonal elements only for the $\dot{\mathbf{d}}_S$ state and \mathbf{v}_k the acceleration input; and $\mathbf{R}_k = 0.10\mathbf{I}$, where \mathbf{I} is a (9, 9) identity matrix.

Identification results for both the S3F and UKF are shown in Figs. 13-21. Fig. 13 shows the top-story displacement response

at Node 20, and Figs. 14–21 present the element section-level responses and the identified values of normalized strength degradation, stiffness degradation, and inelastic transition parameters. All these figures indicate highly effective performance and similar accuracy for both filters. The results varied slightly due to the

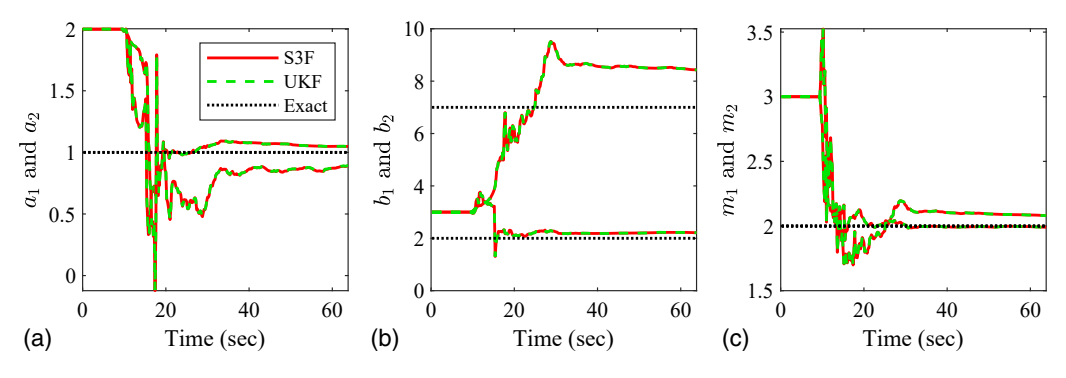


Fig. 9. Hysteretic parameters identification for DOFs 1 and 2.

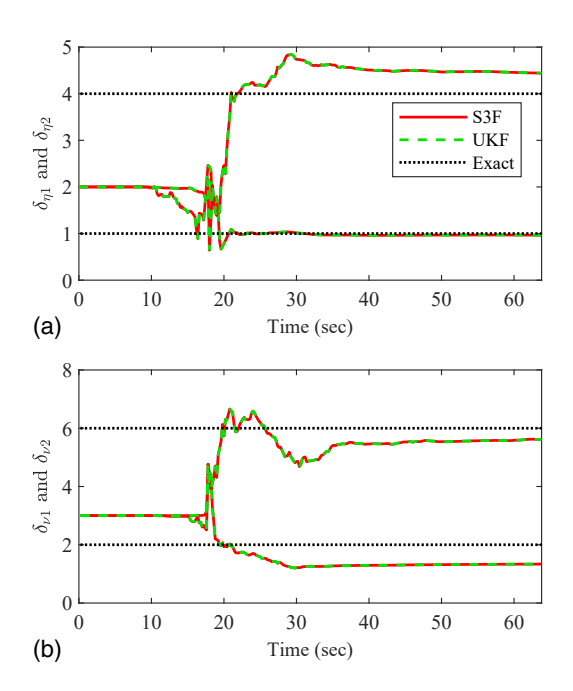


Fig. 10. Stiffness and strength degradation parameters identification for DOFs 1 and 2.

complexity and nonlinearity of the online identification of the highfidelity system presented herein; however, similar identification trends and converged values were found for both filtering estimates. Figs. 14 and 15 show the cross-sectional axial force—axial strain, moment-curvature, shear force-shear strain responses at the start node of the respective elements, as well as the strength degradation (δ_{ν}) , stiffness degradation (δ_{η}) , and inelastic transition (m) parameters for the flexural beam elements, indicated El 16 and El 27, respectively. These elements are referred to as flexural elements because of their long beam length of 6.0 m, resulting in hysteretic energy dissipation primarily due to flexural deformations, with small shear force and shear deformation contributions, as is also evident from the local responses in the figures. Figs. 14 and 15 clearly show the filters' capability for online identification of the complex, interacting, and degrading local nonlinear behaviors. The same local responses and parameters are shown for the sheardominant beam elements, El 17 and El 26, in Figs. 16 and 17, respectively, in which the shear deformation, shear forces, and the corresponding energy dissipation contributions significantly increased due to their reduced beam length of 1.0 m. Therefore, in the shear-dominant beams in Figs. 16 and 17, the peak shear force and shear strains were much larger than those in the flexure-dominant beams, thereby suggesting a significantly different behavior from the long beam elements, with the responses again well predicted by

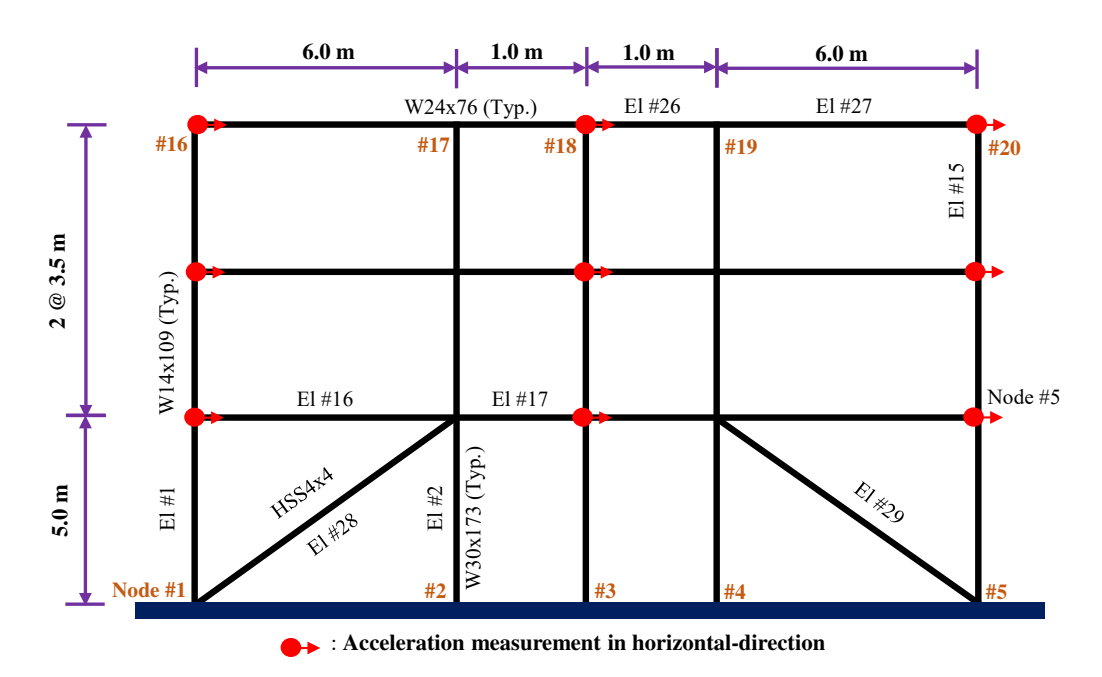


Fig. 11. Steel frame for finite-element model system identification.

both filters. Furthermore, the local axial force–axial strain response and the associated parameters for the brace elements El 28 and El 29 are shown in Figs. 18 and 19, respectively. Based on the a priori engineering knowledge about buckling effects in braces, pinching

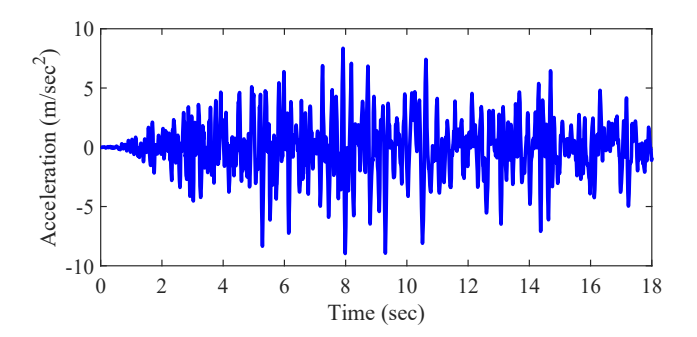


Fig. 12. Base excitation without added noise.

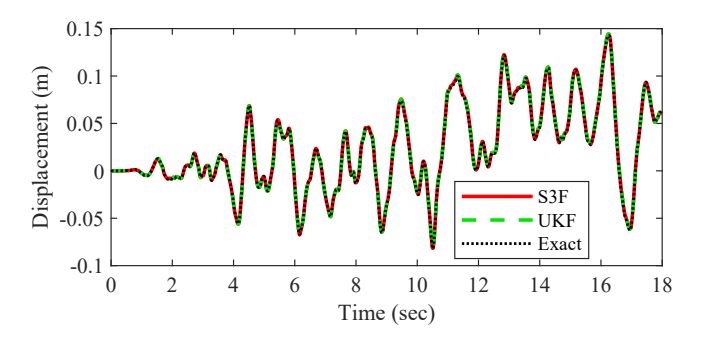


Fig. 13. Top-story displacement response at Node 20 of the steel frame.

and asymmetry is introduced in the axial deformation of the element, based on Amir et al. (2020b). The online performance for the identified dynamic response and the time-invariant parameters was highly accurate (Figs. 18 and 19). Lastly, the local response of the column elements El 12 and El 15 are shown in Figs. 20 and 21, noting that no measurements were taken at either end of El 12. Both of these elements mostly remained in the linear range, and therefore the degradation and inelastic transition parameters were not activated; however, the performance of both elements was again predicted accurately by both filters. Importantly, although the presented framework can simulate and identify a range of behaviors for different element types, the same hysteretic element and finite-element model was applied here for all the elements, including shear-dominant, flexure-dominant, linear, nonlinear, and brace members.

Overall, without prior knowledge of the element behavior, online local responses appropriately identify shear and flexure dominant phenomena, degrading-nondegrading characteristics, and can determine elements that remain linear or not. Because the present modeling enables online state-parameter identification, all the figures presented here refer to the online predicted states and parameters, rather than to simulated results that can be obtained through the converged parameter values.

Summary and Conclusions

An online nonlinear system identification approach, referred to as a scaled spherical simplex filter (S3F), was presented that requires almost 50% less computational effort than the state-of-the-art UKF, yet achieves nearly equivalent accuracy and robustness. The applicability of the presented S3F for any general nonlinear system identification, or any other application for which the UKF can be used, was illustrated through a 20-DOF nonlinear mass–spring–dashpot model numerical example case. The efficiency of the S3F identification scheme was further supported by integrating the filter with a high-fidelity, computationally efficient, and damage plasticity–consistent finite-element framework. The developed finite-element

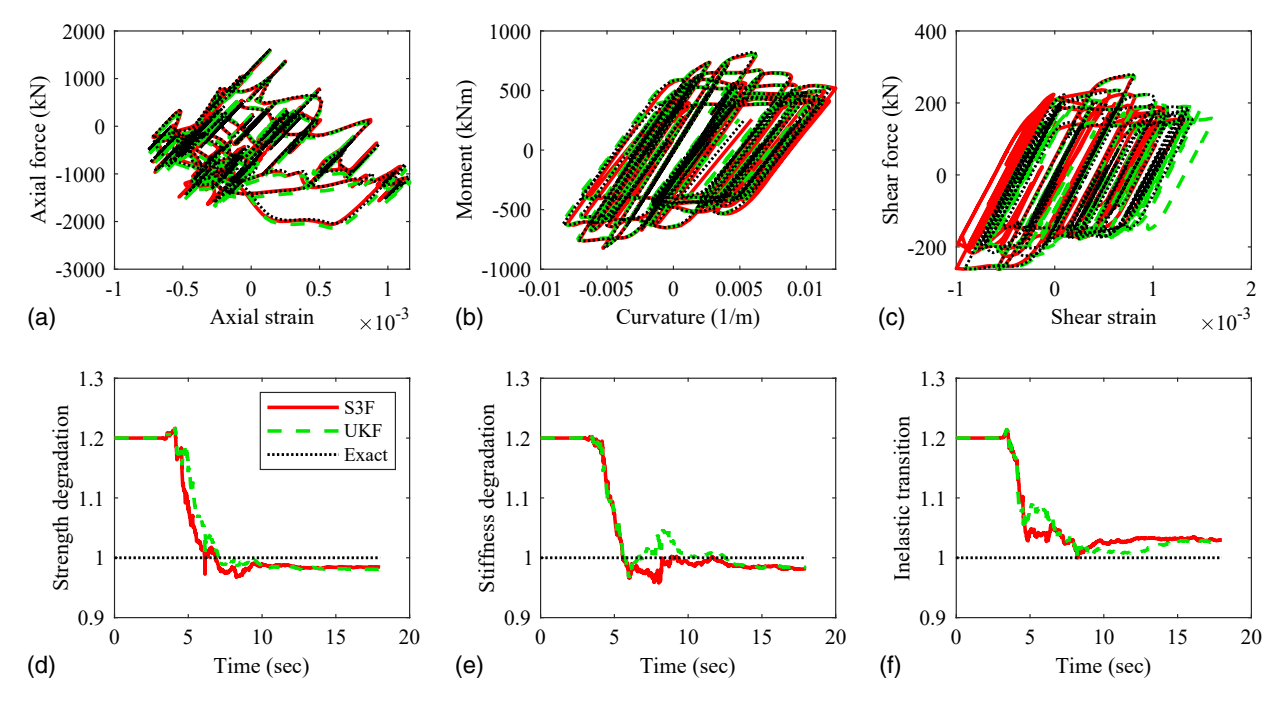


Fig. 14. Local response and parameter predictions for flexure-dominant El 16.

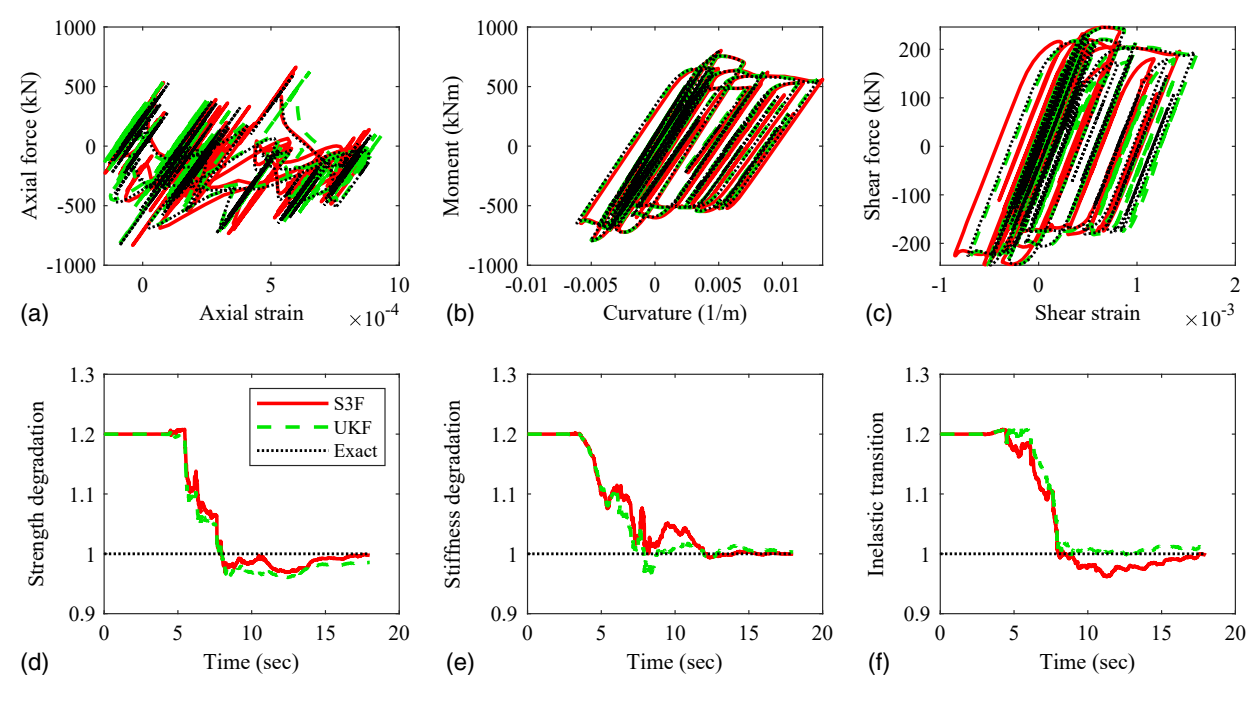


Fig. 15. Local response and parameter predictions for flexure-dominant El 27.

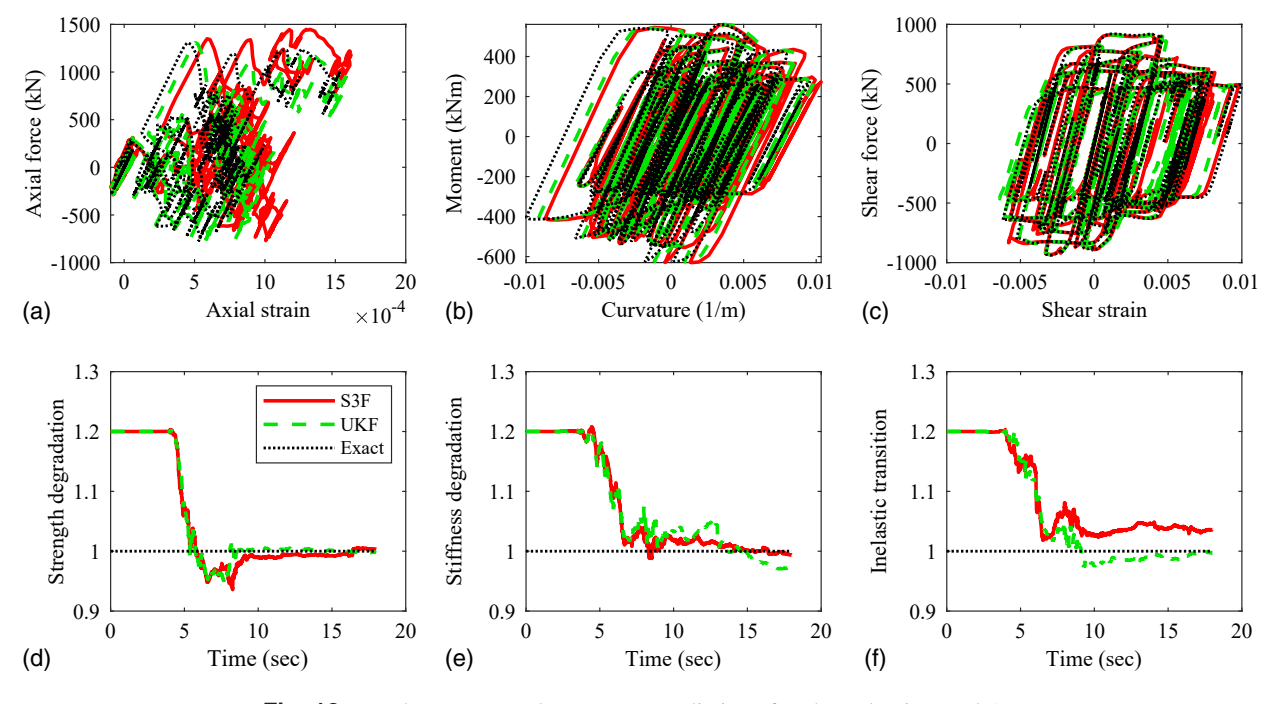


Fig. 16. Local response and parameter predictions for shear-dominant El 17.

model incorporates distributed plasticity effects, degradations, and multiaxial interactions, without requiring any linearization and stiffness updating. The hysteretic finite-element model is particularly well-suited for online identification using filtering approaches due to its implementation similarity to Bouc–Wen-type ODE models, such that the overall system can be presented in a state-space form for joint hidden states and parameters estimation. The efficacy of the finite-element model integration with S3F was presented

through a numerical example case of a realistic steel-frame structure with sparse acceleration measurements, and again the responses were compared with those of the UKF.

Some noteworthy discussion points for the presented finiteelement model identification are summarized as follows:

 Due to the complexity of the finite-element modeling frameworks and the large computational cost associated with their solution schemes, these frameworks are rarely employed for

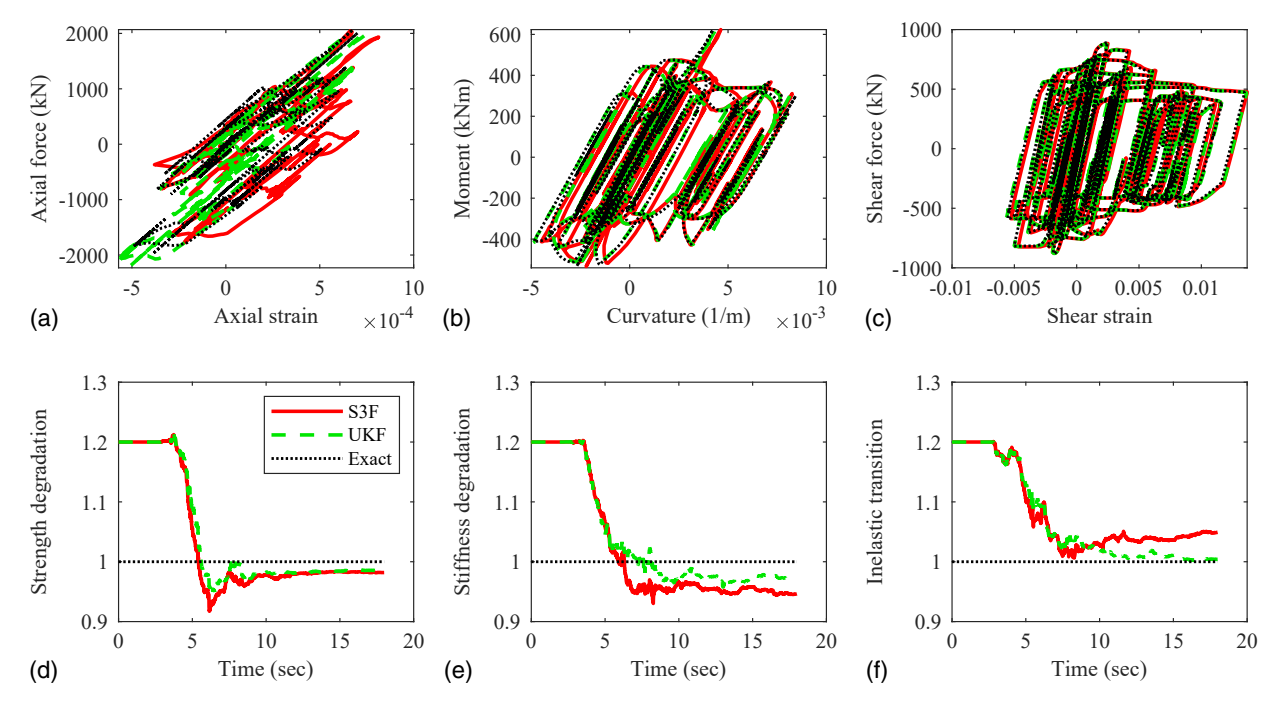


Fig. 17. Local response and parameter predictions for shear-dominant El 26.

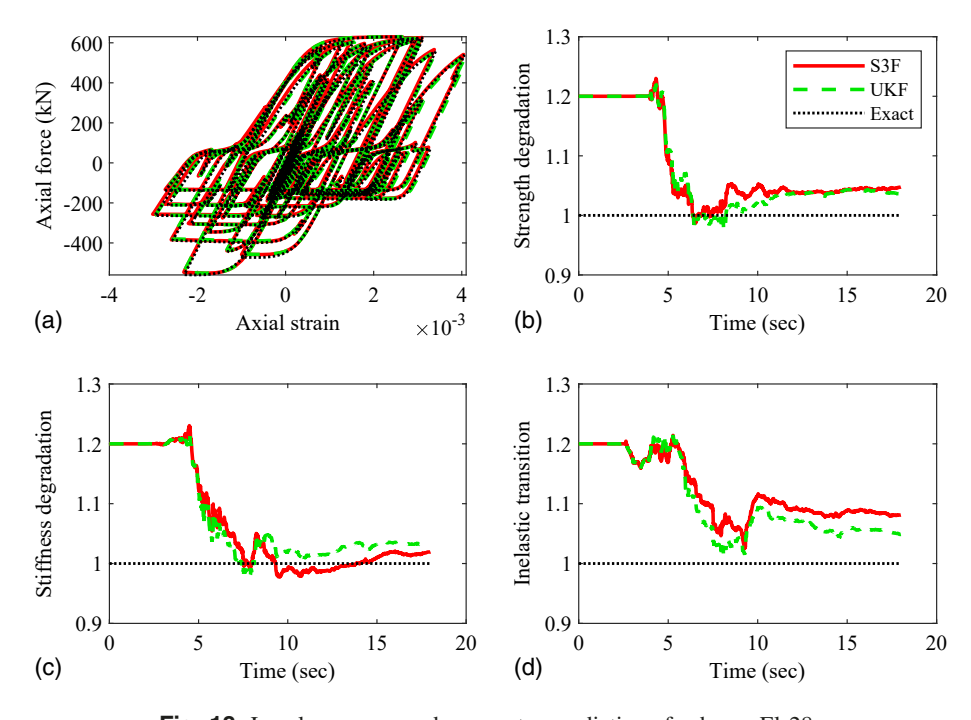


Fig. 18. Local response and parameter predictions for brace El 28.

system identification applications requiring multiple model calls. The present modeling approach aims toward overcoming this limitation and therefore can be applied for filtering.

 The presented approach showcases the model-filter compatibility and potential to simulate and identify complex structural response phenomena owing to the high-fidelity framework considering distributed plasticity, multiaxial interactions, and degradations, while satisfying all the classical plasticity postulates. Together, these attributes have been particularly difficult to integrate in one unified framework, or to identify by conventional methods. Additionally, a single element formulation was implemented here for all structural members and was able to identify a broad range of behaviors, including for shear-dominant, flexural-dominant, linear, nonlinear, and brace elements, among others. The model–filter

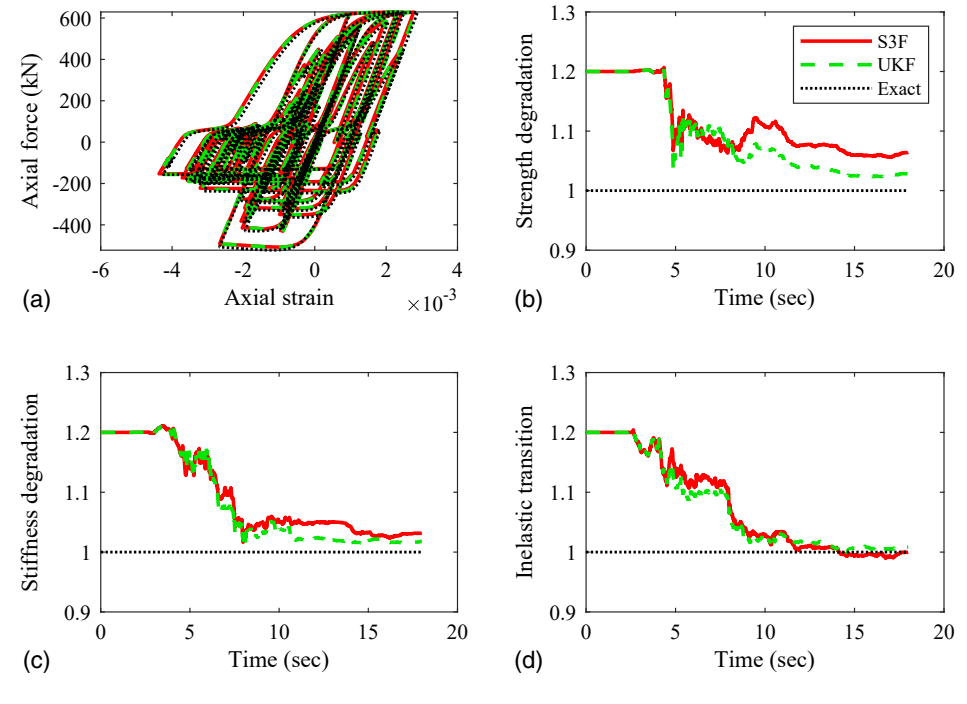


Fig. 19. Local response and parameter predictions for brace El 29.

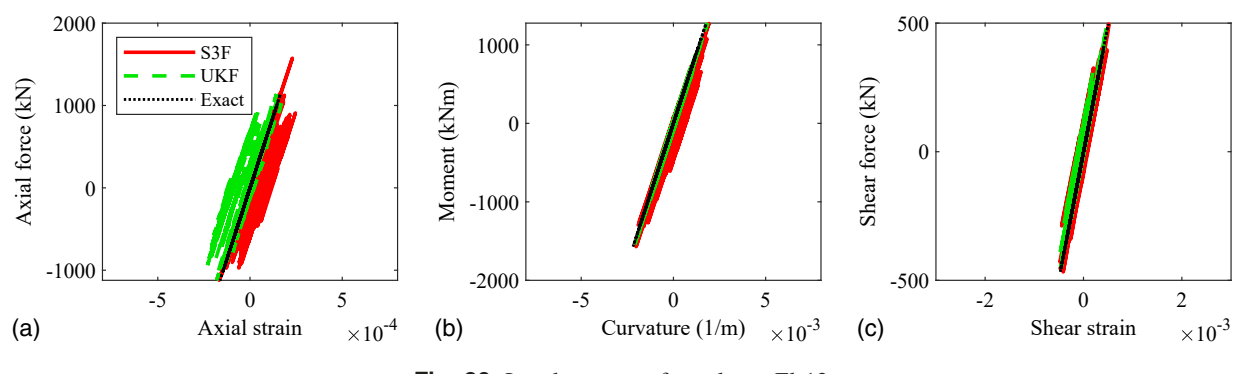


Fig. 20. Local response for column El 12.

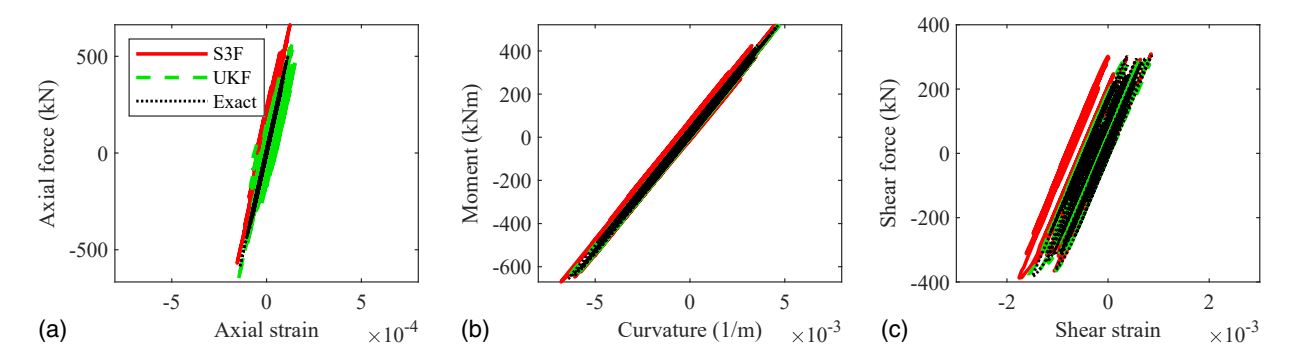


Fig. 21. Local response for column El 15.

integration can thus effectively simulate and identify all these complex element behaviors with a high degree of accuracy.

- 3. The finite-element model identification framework in this work is based on online estimations of hidden states and parameters,
- as shown in the numerical example, thereby enabling real-time identification and damage assessment.
- Overall, this work offers a computationally efficient high-fidelity finite-element model identification framework wherein the S3F

performance was observed to be remarkably good and, as expected, largely similar to that of the UKF, but with only half the computational requirements.

Appendix. Multiaxial Hysteretic Model and Element Matrices

The multiaxial hysteretic model is used as the constitutive law for the hysteretic finite-element formulation and is briefly further presented in this section.

For the coupled degradation-plasticity framework presented herein, the hysteretic laws are derived in the effective stress domain of the classical multiaxial plasticity theory by incorporating strength degradations as scalar damage functions to satisfy the consistency criterion of the yield/capacity surface. The resulting stress—strain relation in the inelastic regime based on the classical multiaxial plasticity (Simo and Hughes 1998) in the effective strain domain (Amir et al. 2020b) is expressed as

$$\dot{\bar{\sigma}} = \mathbf{D}(\dot{\varepsilon} - \dot{\varepsilon}^{p})$$

$$\dot{\bar{\sigma}} = \mathbf{D}\left(\dot{\varepsilon} - \left[\left(\frac{\partial\bar{\Phi}}{\partial\bar{\sigma}}\right)^{T}\mathbf{D}\left(\frac{\partial\bar{\Phi}}{\partial\bar{\sigma}}\right)\right]^{-1}\left(\frac{\partial\bar{\Phi}}{\partial\bar{\sigma}}\right)\left(\frac{\partial\bar{\Phi}}{\partial\bar{\sigma}}\right)^{T}\mathbf{D}\dot{\varepsilon}\right)$$

$$\dot{\bar{\sigma}} = \mathbf{D}(\mathbf{I} - \bar{\mathbf{R}})\dot{\varepsilon}$$
where $\bar{\mathbf{R}} = \frac{\left(\frac{\partial\bar{\Phi}}{\partial\bar{\sigma}}\right)\left(\frac{\partial\bar{\Phi}}{\partial\bar{\sigma}}\right)^{T}\mathbf{D}}{\left(\frac{\partial\bar{\Phi}}{\partial\bar{\sigma}}\right)^{T}\mathbf{D}\left(\frac{\partial\bar{\Phi}}{\partial\bar{\sigma}}\right)}$
(13)

where $\bar{\sigma} = \nu \sigma$ = effective stress vector; ε , ε^e , and ε^p = total, elastic, and plastic strains, respectively; \mathbf{D} = diagonal rigidity matrix; $\bar{\Phi}$ = yield/capacity function, such that $\bar{\Phi} = \Phi(\bar{\sigma})$ is a function of both true stress, σ , and strength degradation, ν , for a system with no hardening; and $\bar{\mathbf{I}}$ and $\bar{\mathbf{R}}$ = identity and interaction matrices, respectively.

Because $\dot{\epsilon}^p$ is 0 in the elastic regime, the stress–strain law is expressed as $\dot{\bar{\sigma}} = D\dot{\epsilon}$ in the corresponding domain. Therefore, instead of employing different expressions depending on the elastic/inelastic and loading/unloading phenomena, the following single vectorized stress–strain law is obtained to satisfy all the aforementioned conditions for both elastic and inelastic regions (Amir et al. 2020b, forthcoming):

$$\dot{\bar{\mathbf{\sigma}}} = \mathbf{D}(\mathbf{I} - \bar{H}_1 \bar{H}_2 \bar{\mathbf{R}}) \dot{\boldsymbol{\varepsilon}} \tag{14}$$

where $\bar{H}_1 = |\bar{\Phi} + 1|^m$ and $\bar{H}_2 = a + b \operatorname{sgn}(\bar{\mathbf{\sigma}}^T \hat{\mathbf{\epsilon}})$ are the appropriate functions, such that either one of them tends to zero in the elastic domain, and both reach a maximum value of 1 in the inelastic domain, thereby satisfying all the conditions of classical plasticity theory through a single expression. Furthermore, by transforming Eq. (14) in terms of true stress, and adding the stiffness degradations and kinematic hardening, the following simplified and concise form is obtained [see Amir et al. (2020b, forthcoming) for details]:

$$\sigma = \bar{\alpha} \mathbf{D} \mathbf{\varepsilon} + (\mathbf{I} - \bar{\alpha}) \mathbf{D} \mathbf{z} \tag{15}$$

$$\dot{\mathbf{z}} = \mathbf{v}^{-1} [(\mathbf{I} - \bar{H}_1 \bar{H}_2 \bar{\mathbf{R}}) \dot{\mathbf{\varepsilon}} - \dot{\mathbf{v}} \mathbf{z}] \tag{16}$$

where Eq. (15) is the hysteretic stress–strain law, in which \mathbf{z} is referred to as a hysteretic deformation vector, and Eq. (16) presents the evolution equation as a set of first-order ODEs. Functions \bar{H}_1 and \bar{H}_2 and matrix $\bar{\mathbf{R}}$ are functions of the effective hysteretic stress, $\bar{\mathbf{\sigma}}^h$, where $\bar{\mathbf{\sigma}}^h = \nu \mathbf{\sigma}^h = \nu (\mathbf{I} - \bar{\mathbf{\alpha}}) \mathbf{D} \mathbf{z}$, and true strain, $\boldsymbol{\varepsilon}$, given by

$$\begin{split} \bar{H}_{1} &= |\Phi(\bar{\mathbf{\sigma}}^{h}) + 1|^{m}; \qquad \bar{H}_{2} = a + b \operatorname{sgn}[(\bar{\mathbf{\sigma}}^{h})^{T} \dot{\mathbf{\epsilon}}] \\ \bar{\mathbf{R}} &= \left[\left(\frac{\partial \Phi(\bar{\mathbf{\sigma}}^{h})}{\partial \bar{\mathbf{\sigma}}^{h}} \right)^{T} \mathbf{D} \left(\frac{\partial \Phi(\bar{\mathbf{\sigma}}^{h})}{\partial \bar{\mathbf{\sigma}}^{h}} \right) \right]^{-1} \left[\left(\frac{\partial \Phi(\bar{\mathbf{\sigma}}^{h})}{\partial \bar{\mathbf{\sigma}}^{h}} \right) \left(\frac{\partial \Phi(\bar{\mathbf{\sigma}}^{h})}{\partial \bar{\mathbf{\sigma}}^{h}} \right)^{T} \mathbf{D} \right] \end{split}$$

$$\tag{17}$$

Eqs. (15) and (16) are the only equations required for all branches of the hysteretic loops, they have the significant attribute that they were derived following the physics of classical multiaxial plasticity, and they can also very compactly incorporate degradation effects and kinematic hardening through a single vectorized ODE expression. In particular, Eq. (16) presents the evolution equation considering coupled degradation-plasticity and full axial-moment–shear interaction. For other, simplified cases, e.g., no interaction or no degradation, evolution equations suggested by Amir et al. (2020b) can also be used readily.

Amir et al. (2020b) also developed a multiaxial degrading hysteretic model for a Timoshenko beam element, in which the stress—strain law of Eq. (15) is expressed in terms of stress resultants at the section level and the corresponding generalized strains, i.e., axial force—centerline axial strain, shear force—shear strain, and moment—curvature. Based on these hysteretic laws, a hysteretic finite-element framework was derived in which the stiffness and hysteretic matrices are constant and evaluated only once at the beginning of the analysis. The derived element stiffness, **K**, and hysteretic, **H**, matrices are as follows:

$$\mathbf{K} = \begin{bmatrix} \frac{\alpha_u A E}{L} & 0 & 0 & -\frac{\alpha_u A E}{L} & 0 & 0\\ 0 & \frac{12\psi_1}{L^3} & \frac{6\psi_1}{L^2} & 0 & -\frac{12\psi_1}{L^3} & \frac{6\psi_1}{L^2}\\ 0 & \frac{6\psi_1}{L^2} & \frac{4\psi_2}{L} & 0 & -\frac{6\psi_1}{L^2} & \frac{2\psi_3}{L}\\ -\frac{\alpha_u A E}{L} & 0 & 0 & \frac{\alpha_u A E}{L} & 0 & 0\\ 0 & -\frac{12\psi_1}{L^3} & -\frac{6\psi_1}{L^2} & 0 & \frac{12\psi_1}{L^3} & -\frac{6\psi_1}{L^2}\\ 0 & \frac{6\psi_1}{L^2} & \frac{2\psi_3}{L} & 0 & -\frac{6\psi_1}{L^2} & \frac{4\psi_2}{L} \end{bmatrix}$$

where $\psi_1 = \alpha_{\phi} \alpha_{\gamma} \mu' EI$; $\psi_2 = \alpha_{\phi} (\alpha_{\gamma} + 3\alpha_{\phi} \lambda) \mu' EI$;

$$\psi_3 = \alpha_{\phi}(\alpha_{\gamma} - 6\alpha_{\phi}\lambda)\mu'EI; \ \mu' = \frac{1}{\alpha_{\gamma} + 12\alpha_{\phi}\lambda}; \ \lambda = \frac{EI}{GA_sL^2}$$
 (18)

$$\mathbf{H} = \begin{bmatrix} -h_{u} & 0 & 0 & -h_{u} & 0 & 0 \\ 0 & -\frac{6h_{\gamma}}{L^{2}} & -\frac{h_{\phi}\alpha_{\gamma}}{L} & 0 & -\frac{6h_{\gamma}}{L^{2}} & \frac{h_{\phi}\alpha_{\gamma}}{L} \\ 0 & -\frac{3h_{\gamma}}{L} & -h_{\phi}(\alpha_{\gamma} + 6\alpha_{\phi}\lambda) & 0 & -\frac{3h_{\gamma}}{L} & -6h_{\phi}\alpha_{\phi}\lambda \\ h_{u} & 0 & 0 & h_{u} & 0 & 0 \\ 0 & \frac{6h_{\gamma}}{L^{2}} & \frac{h_{\phi}\alpha_{\gamma}}{L} & 0 & \frac{6h_{\gamma}}{L^{2}} & -\frac{h_{\phi}\alpha_{\gamma}}{L} \\ 0 & -\frac{3h_{\gamma}}{L} & 6h_{\phi}\alpha_{\phi}\lambda & 0 & -\frac{3h_{\gamma}}{L} & h_{\phi}(\alpha_{\gamma} + 6\alpha_{\phi}\lambda) \end{bmatrix}$$

where
$$h_u = \frac{(1 - \alpha_u)AE}{2}$$
; $h_\phi = (1 - \alpha_\phi)\mu'EI$;
$$h_\gamma = (1 - \alpha_\gamma)\mu'EI\alpha_\phi \tag{19}$$

Hence, based on the constant element matrices in Eqs. (18) and (19), and the evolution equation in Eq. (16), a high-fidelity

hysteretic finite-element model was developed by Amir et al. (2020a, b, forthcoming) that is able to incorporate damage plasticity, multiaxial interactions, and distributed plasticity, and can be presented concisely in a state-space form, similar to hysteretic Bouc–Wen type models, as shown in Table 1 and Eq. (10).

Data Availability Statement

All codes generated during the study are available from the authors by request.

Acknowledgments

This material is based upon work supported by the National Science Foundation under Grant Nos. CMMI-1634575 and CMMI-1751941.

References

- Adurthi, N., P. Singla, and T. Singh. 2018. "Conjugate unscented transformation: Applications to estimation and control." J. Dyn. Syst. Meas. Control 140 (3): 030907. https://doi.org/10.1115/1.4037783.
- Al-Hussein, A., and A. Haldar. 2015. "Novel unscented Kalman filter for health assessment of structural systems with unknown input." *J. Eng. Mech.* 141 (7): 04015012. https://doi.org/10.1061/(ASCE)EM.1943 -7889.0000926.
- Amir, M., K. G. Papakonstantinou, and G. P. Warn. Forthcoming. "State-space formulation for structural analysis with coupled degradation-plasticity and geometric nonlinearity." *J. Struct. Eng.* https://doi.org/10.1061/(ASCE)ST.1943-541X.0003152.
- Amir, M., K. G. Papakonstantinou, and G. P. Warn. 2020a. "A consistent Timoshenko hysteretic beam finite element model." *Int. J. Non Linear Mech.* 119 (Mar): 103218. https://doi.org/10.1016/j.ijnonlinmec.2019.07.003.
- Amir, M., K. G. Papakonstantinou, and G. P. Warn. 2020b. "Hysteretic beam finite-element model including multiaxial yield/capacity surface evolution with degradations." J. Eng. Mech. 146 (9): 04020105. https:// doi.org/10.1061/(ASCE)EM.1943-7889.0001767.
- Astroza, R., H. Ebrahimian, and J. P. Conte. 2015. "Material parameter identification in distributed plasticity FE models of frame-type structures using nonlinear stochastic filtering." *J. Eng. Mech.* 141 (5): 04014149. https://doi.org/10.1061/(ASCE)EM.1943-7889.0000851.
- Astroza, R., H. Ebrahimian, Y. Li, and J. P. Conte. 2017. "Bayesian non-linear structural FE model and seismic input identification for damage assessment of civil structures." *Mech. Syst. Sig. Process.* 93 (Sep): 661–687. https://doi.org/10.1016/j.ymssp.2017.01.040.
- Baber, T. T., and M. N. Noori. 1985. "Random vibration of degrading, pinching systems." *J. Eng. Mech.* 111 (8): 1010–1026. https://doi.org/10.1061/(ASCE)0733-9399(1985)111:8(1010).
- Baber, T. T., and Y.-K. Wen. 1981. "Random vibration hysteretic, degrading systems." *J. Eng. Mech. Div.* 107 (6): 1069–1087. https://doi.org/10.1061/JMCEA3.0002768.
- Bathe, K. J. 2014. Finite element procedures. Watertown, MA: Klaus-Jurgen Bathe.
- Bouc, R. 1967. "Forced vibrations of mechanical systems with hysteresis." In *Proc.*, 4th Conf. on Nonlinear Oscillations. Prague, Czech Republic: Czechoslovak Academy of Sciences, Dept. of Radio Engineering and Electronics.
- Calabrese, A., S. Strano, and M. Terzo. 2018. "Adaptive constrained unscented Kalman filtering for real-time nonlinear structural system identification." *Struct. Control Health Monit.* 25 (2): e2084. https://doi.org/10.1002/stc.2084.
- Chatzi, E. N., A. W. Smyth, and S. F. Masri. 2010. "Experimental application of on-line parametric identification for nonlinear hysteretic systems with model uncertainty." *Struct. Saf.* 32 (5): 326–337. https://doi.org/10.1016/j.strusafe.2010.03.008.

- Chatzis, M. N., and E. N. Chatzi. 2017. "A discontinuous unscented Kalman filter for non-smooth dynamic problems." Front. Built Environ. 3 (Oct): 56. https://doi.org/10.3389/fbuil.2017.00056.
- Chatzis, M. N., E. N. Chatzi, and A. W. Smyth. 2015. "On the observability and identifiability of nonlinear structural and mechanical systems." *Struct. Control Health Monit.* 22 (3): 574–593. https://doi.org/10.1002/stc.1690
- Deierlein, G. G., A. M. Reinhorn, and M. R. Willford. 2010. Nonlinear structural analysis for seismic design. NEHRP Seismic Design Technical Brief No. 4. Gaithersburg, MD: NIST.
- Erazo, K., and E. M. Hernandez. 2016. "Bayesian model-data fusion for mechanistic postearthquake damage assessment of building structures." J. Eng. Mech. 142 (9): 04016062. https://doi.org/10.1061/(ASCE)EM .1943-7889.0001114.
- Filippou, F. C., and G. L. Fenves. 2004. "Methods of analysis for earthquake-resistant structures." Chap. 6 of *Earthquake engineering:* From engineering seismology to performance-based engineering, 6. Boca Raton, FL: CRC Press.
- Foliente, G. C. 1995. "Hysteresis modeling of wood joints and structural systems." *J. Struct. Eng.* 121 (6): 1013–1022. https://doi.org/10.1061/(ASCE)0733-9445(1995)121:6(1013).
- Gendy, A. S., and A. F. Saleeb. 1993. "Generalized yield surface representations in the elasto-plastic three-dimensional analysis of frames." *Comput. Struct.* 49 (2): 351–362. https://doi.org/10.1016/0045-7949(93)90114-S.
- Gordon, N. J., D. J. Salmond, and A. F. M. Smith. 1993. "Novel approach to nonlinear/non-Gaussian Bayesian state estimation." *IEE Proc. F* (*Radar Signal Process.*) 140 (2): 107–113. https://doi.org/10.1049/ip -f-2.1993.0015.
- Ismail, M., F. Ikhouane, and J. Rodellar. 2009. "The hysteresis Bouc-Wen model, a survey." Arch. Comput. Methods Eng. 16 (2): 161–188. https://doi.org/10.1007/s11831-009-9031-8.
- Julier, S., and J. K. Uhlmann. 1996. A general method for approximating nonlinear transformations of probability distributions. Oxford, UK: Robotics Research Group, Dept. of Engineering Science, Univ. of Oxford.
- Julier, S. J. 1998. "Skewed approach to filtering." In Vol. 3373 of Signal and data processing of small targets, 271–282. Bellingham, WA: International Society for Optics and Photonics.
- Julier, S. J. 2002. "The scaled unscented transformation." In Vol. 6 of Proc., of the 2002 American Control Conf., 4555–4559. New York: IEEE.
- Julier, S. J. 2003. "The spherical simplex unscented transformation." In Vol. 3 of *Proc.*, of the 2003 American Control Conf., 2430–2434. New York: IEEE.
- Julier, S. J., and J. K. Uhlmann. 1997. "New extension of the Kalman filter to nonlinear systems." In Vol. 3068 of Signal processing, sensor fusion, and target recognition VI, 182–193. Bellingham, WA: International Society for Optics and Photonics.
- Julier, S. J., and J. K. Uhlmann. 2002. "Reduced sigma point filters for the propagation of means and covariances through nonlinear transformations." In Vol. 2 of *Proc.*, of the 2002 American Control Conf., 887–892. New York: IEEE.
- Julier, S. J., and J. K. Uhlmann. 2004. "Unscented filtering and non-linear estimation." *Proc. IEEE* 92 (3): 401–422. https://doi.org/10.1109/JPROC.2003.823141.
- Julier, S. J., J. K. Uhlmann, and H. F. Durrant-Whyte. 1995. "A new approach for filtering nonlinear systems." In Vol. 3 of *Proc.*, of 1995 American Control Conf., 1628–1632. New York: IEEE.
- Kachanov, L. 1958. "Time of the rupture process under creep conditions." Izv. Akad. Nauk SSSR Otdelenie Tekniches. 8: 26–31.
- Kachanov, M. 1980. "Continuum model of medium with cracks." J. Eng. Mech. 106 (5): 1039–1051. https://doi.org/10.1061/JMCEA3.0002642.
- Kontoroupi, T., and A. W. Smyth. 2016. "Online noise identification for joint state and parameter estimation of nonlinear systems." ASCE-ASME J. Risk Uncertainty Eng. Syst. Part A: Civ. Eng. 2 (3): B4015006. https:// doi.org/10.1061/AJRUA6.0000839.
- Lei, Y., D. Xia, K. Erazo, and S. Nagarajaiah. 2019. "A novel unscented Kalman filter for recursive state-input-system identification of nonlinear systems." *Mech. Syst. Sig. Process.* 127 (Jul): 120–135. https://doi.org /10.1016/j.ymssp.2019.03.013.

- Lemaitre, J. 1996. A course on damage mechanics. New York: Springer. Lignos, D. G., and H. Krawinkler. 2011. "Deterioration modeling of steel components in support of collapse prediction of steel moment frames under earthquake loading." J. Struct. Eng. 137 (11): 1291–1302. https:// doi.org/10.1061/(ASCE)ST.1943-541X.0000376.
- Olivier, A., and A. W. Smyth. 2017. "Review of nonlinear filtering for SHM with an exploration of novel higher-order Kalman filtering algorithms for uncertainty quantification." *J. Eng. Mech.* 143 (11): 04017128. https://doi.org/10.1061/(ASCE)EM.1943-7889.0001276.
- Papakonstantinou, K. G., M. Amir, and G. P. Warn. 2022. "A scaled spherical simplex filter (S3F) with a decreased *n*+2 sigma points set size and equivalent 2*n*+1 unscented Kalman filter (UKF) accuracy." *Mech. Syst. Sig. Process* 163: 107433. https://doi.org/10.1016/j.ymssp.2020.107433.
- Papakonstantinou, K. G., P. C. Dimizas, and V. K. Koumousis. 2008. "An inelastic beam element with hysteretic damping." *Shock Vib.* 15 (3–4): 273–290. https://doi.org/10.1155/2008/707419.
- Scott, M. H., G. L. Fenves, F. McKenna, and F. C. Filippou. 2008. "Software patterns for nonlinear beam-column models." *J. Struct. Eng.* 134 (4): 562–571. https://doi.org/10.1061/(ASCE)0733-9445(2008)134:4(562).
- Simo, J., and T. Hughes. 1998. Computational inelasticity. New York: Springer.
- Sivaselvan, M. V., and A. M. Reinhorn. 2000. "Hysteretic models for deteriorating inelastic structures." *J. Eng. Mech.* 126 (6): 633–640. https://doi.org/10.1061/(ASCE)0733-9399(2000)126:6(633).
- Song, M., R. Astroza, H. Ebrahimian, B. Moaveni, and C. Papadimitriou. 2020. "Adaptive Kalman filters for nonlinear finite element model updating." *Mech. Syst. Sig. Process.* 143 (Sep): 106837. https://doi.org/10 .1016/j.ymssp.2020.106837.
- Song, W. 2018. "Generalized minimum variance unbiased joint input-state estimation and its unscented scheme for dynamic systems with direct feedthrough." *Mech. Syst. Sig. Process.* 99 (Jan): 886–920. https://doi.org/10.1016/j.ymssp.2017.06.032.
- Song, W., and S. Dyke. 2014. "Real-time dynamic model updating of a hysteretic structural system." J. Struct. Eng. 140 (3): 04013082. https:// doi.org/10.1061/(ASCE)ST.1943-541X.0000857.
- Spacone, E., F. C. Filippou, and F. F. Taucer. 1996. "Fibre beam-column model for non-linear analysis of RC frames: Part I. Formulation."

- Earthquake Eng. Struct. Dyn. 25 (7): 711–725. https://doi.org/10.1002 /(SICI)1096-9845(199607)25:7<711::AID-EQE576>3.0.CO;2-9.
- Tenne, D., and T. Singh. 2003. "The higher order unscented filter." In Vol. 3 of *Proc.*, 2003 American Control Conf., 2441–2446. New York: IEEE.
- Triantafyllou, S. P., and V. K. Koumousis. 2011. "An inelastic Timoshenko beam element with axial–shear–flexural interaction." *Comput. Mech.* 48 (6): 713–727. https://doi.org/10.1007/s00466-011-0616-3.
- Triantafyllou, S. P., and V. K. Koumousis. 2012. "Small and large displacement dynamic analysis of frame structures based on hysteretic beam elements." *J. Eng. Mech.* 138 (1): 36–49. https://doi.org/10.1061/(ASCE) EM.1943-7889.0000306.
- van der Merwe, R. 2004. "Sigma-point Kalman filters for probabilistic inference in dynamic state-space models." Ph.D. dissertation, OGI School of Science and Engineering, Oregon Health & Science Univ.
- Vlachos, C., K. G. Papakonstantinou, and G. Deodatis. 2018. "Predictive model for site specific simulation of ground motions based on earthquake scenarios." *Earthquake Eng. Struct. Dyn.* 47 (1): 195–218. https://doi.org/10.1002/eqe.2948.
- Wan, E. A., and R. van Der Merwe. 2000. "The unscented Kalman filter for nonlinear estimation." In Proc., of the IEEE 2000 Adaptive Systems for Signal Processing, Communications, and Control Symp., 153–158. New York: IEEE.
- Wang, C.-H., G. C. Foliente, M. V. Sivaselvan, and A. M. Reinhorn. 2001. "Hysteretic models for deteriorating inelastic structures." *J. Eng. Mech.* 127 (11): 1200–1202. https://doi.org/10.1061/(ASCE)0733-9399(2001) 127:11(1200).
- Wen, Y.-K. 1976. "Method for random vibration of hysteretic systems." J. Eng. Mech. Div. 102 (2): 249–263. https://doi.org/10.1061/JMCEA3 .0002106.
- Wu, M., and A. Smyth. 2008. "Real-time parameter estimation for degrading and pinching hysteretic models." *Int. J. Non Linear Mech.* 43 (9): 822–833. https://doi.org/10.1016/j.ijnonlinmec.2008.05.010.
- Xie, Z., and J. Feng. 2012. "Real-time nonlinear structural system identification via iterated unscented Kalman filter." *Mech. Syst. Sig. Process*. 28 (Apr): 309–322. https://doi.org/10.1016/j.ymssp.2011.02.005.
- Yun, C.-B., and M. Shinozuka. 1980. "Identification of nonlinear structural dynamic systems." J. Struct. Mech. 8 (2): 187–203. https://doi.org/10 .1080/03601218008907359.